Master's thesis

NTNU
Norwegian University of Science and Technology
Faculty of Engineering
Department of Energy and Process Engineering

Jonas Trygve Aannestad

Numerical investigation of lean premixed ammonia/hydrogen/ nitrogen-air flame at blow-out

Master's thesis in MTPROD
Supervisor: Andrea Gruber
December 2023

NTNU
Norwegian University of
Science and Technology

Jonas Trygve Aannestad

Numerical investigation of lean premixed ammonia/hydrogen/nitrogen-air flame at blow-out

Master's thesis in MTPROD
Supervisor: Andrea Gruber
December 2023

Norwegian University of Science and Technology
Faculty of Engineering
Department of Energy and Process Engineering

NTNU
Norwegian University of
Science and Technology

Abstract

In this thesis, a Large-Eddy Simulation (LES) study of turbulent flames at blow-out taking place in a bluff-body burner is conducted. The thesis aims to assess the ability of OpenFOAM's solver for turbulent reactive flow to recreate the blow-out behavior of lean, premixed CH_4-air flame and $NH_3/H_2/N_2$-air flame as observed experimentally. Experimentally, the flames experience blow-out at different velocities, differing by an order of magnitude, despite having nominally-identical laminar flame characteristics. This is due to thermodiffusive instabilities caused by H_2 in the mixture, which accelerates flame front propagation. This results in increased heat release rate and blow-out resilience. In the numerical study, the Partially-Stirred Reactor model was employed to model turbulence-chemistry interaction, along with three different reaction mechanisms. The numerical setup recreates the blow-out velocity of CH_4-air flame within 10% error of reference experiment, while the $NH_3/H_2/N_2$-air flame underpredicts the blow-out velocity by an order of magnitude. Reaction mechanisms are shown to be very influential, while the thesis concludes that the thermo-diffusive physics of the H_2 mixture is not captured by OpenFOAM's Fickian molecular transport.

Acknowledgement

I would like to express my gratitude to my supervisor Andrea Gruber for allowing me to take on this challenging project, while supporting and pushing me to learn and explore. I truly feel that working on this thesis has been a privilege for me. You have given me deep insights and inspired a pragmatic approach to a very broad and difficult field. I am very grateful and honored to have you as my supervisor. I also want to thank the IT-department at EPT NTNU, especially Eugen Uthaug, for ensuring that I always had access to the tools needed for conducting this thesis.

Contents

List of Figures

List of Tables

1 Background motivation

1.1 Introduction

Combustion is crucial for providing power and electricity to society and industry. In 2018, an estimated 23.1 % of electricity generation came from natural gas [1]. While modern gas turbines and other power generators running on fossil fuels are effective, they release unwanted emissions, like CO_2 and NO_x gases. IEA reported that 20.6 % of global green house gas emissions from the energy sector in 2018 stemmed from natural gas. The increasing demand for clean, efficient, and reliable power to meet sustainability goals and power demand pushes engineers and researchers to find new ways to generate more power while reducing emissions. Due to the significant share of electricity and power coming from gas turbines, the reduction of emissions from gas turbines has received significant attention from industry and research institutions. Development of new low- or zero-emission gas turbines faces multiple challenges that are unique with these fuels, as will be explained in section 1.1.1, which have implications for the operational flexibility, as explained in section 1.1.2. To overcome and solve these challenges, significant time and resources must be used. Digital simulation and analysis tools can help accelerate the development of physical testing these new gas turbines, through providing sufficiently accurate performance prediction and recreating of physical behaviour without the need for physically building prototypes. While the tools will not directly replace prototypes, it can aid in separating bad solutions from promising solutions, and hence reduce the risk of prototype campaigns. In order for simulation tools to provide any value to the development projects, they need to be sufficiently accurate. The tools must not only be accurate for nominal, steady-state operation of a gas turbine, but ideally over a wide range of operational conditions, including extreme events like blow-out in the combustion chamber, as described in detail in 1.1.2. Simulation techniques that can accurately predict the occurrence of such events, will enable faster development of new low-emission gas turbines. With this motivation, this thesis sets out to investigate the capability of numerical simulation of a lean, premixed, turbulent ammonia/hydrogen/nitrogen-air flame at blowout conditions. The thesis will recreate the experiment as described by Wiseman et al. 2021 [2] in the computational fluid dynamics software OpenFOAM, and analyze the quantitative and qualitative discrepancies between the experiment and the simulation.

1.1.1 Differential diffusion in lean premixed flames

In an attempt to reduce carbon-based emissions from combustion processes, carbon-free fuels, such as H_2 and NH_3, are researched. Transitioning from carbon-based to carbon-free fuels will significantly reduce the direct carbon-based emissions from gas turbines. However, many properties of carbon-free fuels differ significantly from carbon-based fuels. While gas turbines are fuel-flexible on paper, the burner geometry is, in reality, designed around a specific fuel and its properties, due to the need for high performance and reliable gas turbines. Designing a gas turbine that does not utilize carbon-based fuels challenges the decades of industrial experience and scientific knowledge regarding design, development, commissioning, and operation of gas turbines. To ensure a successful transition to carbon-free fuels, significant research efforts remain before carbon-free gas turbines become technically relevant and economically competitive in the short term with the current state-of-the-art carbon-based gas turbines.

H_2 is a high-performing fuel, containing a Lower Heating value of 120 MJ/kg [3], and is highly reactive. It has a high flammability range, which enables operational flexibility. This high performance does come with its practical downsides. H_2 has an incredibly low density, necessitating storage and transportation at either very high pressure or incredibly low temperatures to reduce the total space used by an H_2-system. Due to its high reactivity, H_2 difficult to stabilize during combustion processes [4], [5], [6]. A solution would then be to have a molecule that carries H_2 in a more practical way and stabilizes combustion, without sacrificing too much in terms of performance or emissions.

NH_3 has been used in gas turbines previously, but due to low performance and reactivity, has been relegated to the role of a supplementary fuel in addition to the traditional carbon-based fuels. The flammability range is close to the stability limits, and burn time is slow. Density and other practical aspects are, however, much better than H_2. Additionally, NH_3 is one of the most produced chemicals in the world at the moment [7]. This has a very positive effect on the economic aspect of carbon-free fuels and also implies that there is significant industrial experience with producing, handling, transporting, and storing NH_3, which reduces the risk of NH_3-related projects. The ultimate carbon-free fuel combines the combustion properties of H_2 and the transport and storage properties of NH_3. This has led researchers to investigate the use of NH_3 as an H_2 carrier, where waste heat from the combustion process is used to decompose NH_3 into H_2 and N_2.

The addition of H_2 complicates the mechanism of turbulent combustion. While the impact of molecular diffusion for more traditional carbon-based fuels reduces as the degree of turbulence

increases in combustion, the molecular diffusion of H_2 seems to be rate-controlling for premixed combustion [8], even in flames with a very high degree of turbulence. This is due to the differential diffusion of the H_2 and H molecules, which indicates that in a mix of species, the H_2 and H molecules will diffuse much faster than the other species in the mix. Moreover, H_2 and H molecules are special because of their Lewis number (Le):

$$Le = \frac{\alpha}{\mathcal{D}} \tag{1.1}$$

where α is the thermal diffusivity and $\mathcal{D}$ is the mass diffusivity.

The differential diffusion can cause locally higher equivalence ratios, ϕ, throughout the flame front. This happens as diffusion happens normal to the flame front surface. Concave curvatures (with respect to the product side) in the flame front will then create focus areas, causing diffusion to transport molecules to the same point in space and hence raise the local concentration. The higher degree of concaveness causes more molecules to diffuse into a smaller location, raising the local concentration of the diffused species. Since $Le_{H_2} \leq 0.3$ [8], H_2 and H molecules will diffuse towards the product zone (where Y_{H_2} is relatively small) faster than the heat manages to propagate towards the reactant zone, causing the illusion of H_2 to diffuse "through" the flame front, towards the combustion process. In a fuel-lean environment, this will raise the local eqauivlence ratio ϕ. The local ϕ increases laminar flame speed. Laminar flame speed describes how fast the flame front propogates forward in space throughout premixed reactants. Because of differential diffusion, local ϕ is a consequence of local flame front geometry, causing locally faster propagation of the flame front, which further deforms the flame front in a way that again causes locally higher ϕ. This becomes a self-exciting mechanism, drastically increasing flame front surface, deformation, and spatial propagation. This is found to be a rate control mechanism in turbulent premixed flames, which increases the heat release rate (HRR) [8] and the resistance to blow-out [2].

1.1.2 Lean Blow-Out

Reducing emissions of NO_x gases in gas turbines is achievable by lowering the combustion temperature below their formation temperature. This is achieved through the use of lean fuel mixtures, which introduce an excess of air, relative to stoichiometric ratios, to dilute the heat generated during combustion, consequently decreasing the temperature within the combustion chamber. However, there is a delicate balance in this process. Excess dilution can lead to flame extinction, as the combustion process requires a minimum temperature for self-sustainment.

To counteract this, engineers employ a simple yet effective technique involving flame holders within the combustion chamber; geometries that stabilize the flame spatially and temporally. One example of a flame holder is bluff bodies. These bluff bodies create a wake that holds a hot recirculation zone, containing the products of combustion, which serve as an ignition source for incoming fresh reactants. Upon contact, these reactants ignite, resulting in a flame that surrounds the recirculation zone, as depicted in schematic 1. The thin zone between the cold reactant stream and hot product recirculation zone is where a distinct majority of the heat release occurs. This zone will hence forth be referred to as the flame front. To further ensure low NO_x emissions, a strategy known as premixing is adopted. In this approach, reactants are mixed upstream of the combustion chamber, aiming to prevent stochastic mixing scenarios where localized high fuel concentrations create "hot spots" capable of reaching the NO_x formation temperature.

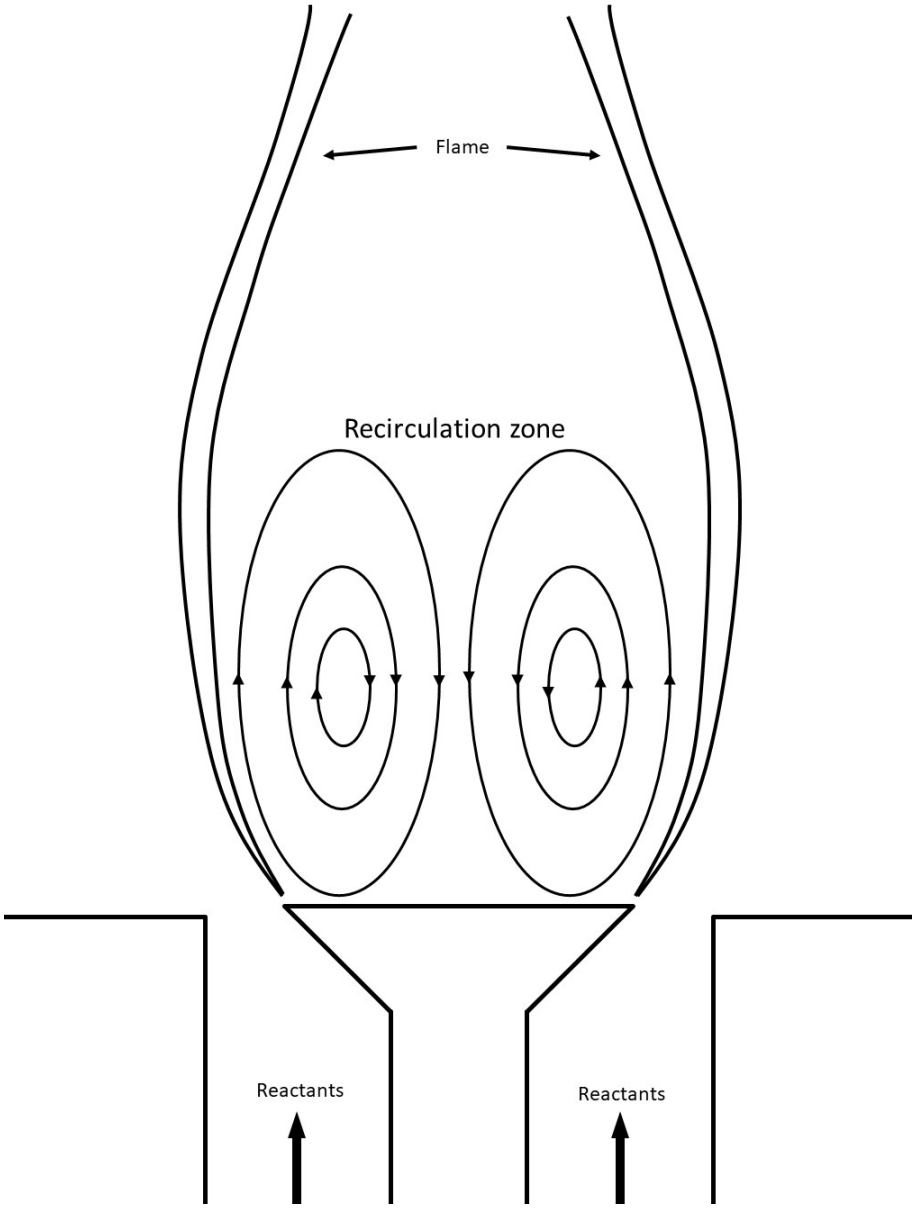

Figure 1. Schematic of a bluff body stabilized flame and adhering recirculation zone.

Lean flames are prone to extinguishing, limiting the operating range of gas turbines. One way for the flame to extinguish is through blowout, where a too high flow velocity past the flame holder causes the flame to dettach from the flame holder and extinguish. Blowout is not fully understood, and has received a lot of attention in literature over the years, as covered in sec. 1.2.

A similar phenomena is blow*off*, where the flame is extinguished while attached to the flame holder. The distinction between blow*out* and blow*off* is described by Mansour (2003) [9], but the distinction is not followed in this thesis, and will use the terms as equivalent statements. This is because the thesis only deals with attached flames, and so the distinction falls beyond the scope of this thesis. Neither blow-off nor blow-out should be confused with local extinction,

as Shanbhogue et al. (2009) [10], which should be considered as an event during the blow-out.

Lieuwen (2012) [11] described the blow-out as a two-stage process: First, local flame exctintion appears, where, usually in high strain-rate regions, the local combustion process ceases to continue, leaving a hole in the flame front. The local combustion process can resume, mending the hole in the flame front. Decreasing the lean fuel-ratio or increasing flow velocities will increase occurance of local extinction. Secondly, global extinction occures. Global extinction is starts off with increasingly unsteady and chaotic wake behind the flame, that eventually progresses upstream and causes severe flame flapping. This destabilizes the flame, causing global flame extinction

1.2 Literature review

Research into the utilization of bluff bodies for flame stabilization has garnered substantial attention in conjunction with the development of gas turbine technology. This focus primarily arises due to the applicability of bluff body stabilization in compact combustor designs. Consequently, investigations in this domain frequently explore the blockage ratio, denoting the ratio between the cross-sectional area of the bluff body and the flow cross-section, as a variable that exerts a discernible influence on flame stability.

In 1953, presented J.P. Longwell a comprehensive review paper [12]. Although this publication identified crucial phenomena like the recirculation zone, it did not definitively establish a correlation between blow-off limits and other relevant parameters. During this era, analyses suggested that the blowout limit for a specific equivalence ratio (ϕ) was intricately linked to the parameter $Up^aD^bT^c$, where U signified the mixture velocity upon passing the flame holder, p represented the combustor pressure, D denoted the characteristic dimension of the stabilizer, and T indicated temperature. The constants a, b, and c remained subjects of ongoing debate and investigation.

Building upon Longwell's work, M.V. Herbert conducted a survey in 1960 [13] to examine more recent data pertaining to the aerodynamic impact on flame stabilization. This endeavor led to the postulation of a fundamental connection between the chemical reaction rate and the Reynolds number. Notably, this relationship implicated the Damköhler number (Da), which represents the ratio between transport timescales (τ_{trans}) and chemical timescales (τ_{chem}).

$$Da = \frac{\tau_{trans}}{\tau_{chem}} \tag{1.2}$$

The theory proposing a dependence of blowout limits on the Damköhler number (Da) gained further substantiation through the work of S.L. Plee and A.M. Mellor in 1979 [14]. Their experiments unequivocally identified a critical Da value that delineated the blowout limit. It's noteworthy that the timescales considered in their research were explicitly confined to the shear layer within the recirculation zone. However, one of the persistent challenges associated with unraveling the dependence of blowout limits on Da lies in the selection of the appropriate chemical timescale (τ_{chem}). Potter and Wong's study [15] underscored the inadequacy of the time-to-ignite (τ_{ign}) as the correct timescale, despite variations in τ_{ign} across different tested hydrocarbon fuels.

In 1991, S. J. Shanbhogue et al. [10] made significant contributions by proposing the use of the chemical timescale of a perfectly stirred reactor (τ_{PSR}) in establishing a distinct relationship

between Da and Re_D for two-dimensional bluff bodies. However, this relationship's applicability weakened when applied to axisymmetric bluff bodies.

In 1991, the work of Radhakrishnan et al. [16] advocated for the use of streamwise velocity at the plane of maximum bluff body diameter (referred to as $\mathbf{u}_{\text{lip}}$) as a more suitable characteristic velocity than the upstream velocity. Furthermore, they postulated that the length of the recirculation zone could serve as a superior characteristic length parameter, although establishing an explicit *a priori* relation between bluff body geometry and the blowout limit remained elusive.

In 1992, J.C. Pan and D.R. Ballal [17] delved into the effects of turbulence and equivalence ratio on lean premixed flames. Their investigations unveiled that increasing turbulence intensity or approaching stoichiometric equivalence ratios led to a shortening of the recirculation zone. This shortening was intrinsically linked to the reaction rate, as heightened turbulence intensity and stoichiometric conditions accelerated the reaction rate, subsequently affecting the recirculation zone's length. Their research also brought to light the presence of excess cold reactants in lean flame blowout scenarios, triggered by entrainment mechanisms. The gradients in the flame front induced by these cold reactants escalated the entrainment process and eventually extinguished the flame. This phenomenon underscored the role of turbulence in blowout events.

The existence of cold reactants further underscored the notion that blowout hinges on an imbalance within the recirculation zone. Whether it be the rate of entrainment surpassing the reactant consumption rate [18] or the heat release from combustion falling short of the heating requirement for igniting incoming cold reactants [19], these factors contributed to blowout. This perspective found reinforcement in observations of recirculation zone temperature diminishing as $\mathbf{u}_{\text{lip}}$ approached its blowout threshold [20].

In 2011, J.R. Dawson et al. [21] provided visual insights into blowout events within a lean premixed methane flame. Their experiments, involving the real-time imaging of the instantaneous OH distribution, unveiled distinctive characteristics. As blowout approached, the flame exhibited pronounced shortening and a reduction in the angle between the flame front and the incoming flow at the bluff body's lip. Further downstream, the flame narrowed progressively, eventually conforming to the sharp curvature of the recirculation zone's crest, assuming an "M-shape" configuration. This visual depiction elucidated the upstream flow of cold reactants into the recirculation zone, primarily originating from the recirculation zone's downstream section. Just before blowout occurred, flames were observed within the recirculation zone. The study postulated that the diminishing flame and recirculation zone dimensions, coupled with

reduced combustion volume, collectively restricted the available heat for sustaining combustion, ultimately culminating in flame extinction. Turbulence-induced fragmentation further contributed to flame extinction. Remarkably, their research highlighted the stochastic nature of blowout events, occasionally leading to flame extinction before reaching the absolute limit, thus emphasizing turbulence's role in blowout.

Additionally, the paper underscored the significance of the effective Lewis number (Le) of the reactant mixture in dictating the blowout mechanism. For methane-air flames characterized by $Le < 1$, extinction resulted from heat loss due to the intrusion of cold reactants into the recirculation zone, amplified by turbulence. In contrast, for more complex hydrocarbons with $Le > 1$, local extinction could be induced by strain. These findings provided valuable insights into the multifaceted nature of blowout phenomena.

Quantitative data from the same experiment conducted by J. Kariuki et al. in 2012 [22] further validated the previously observed "M-shape" and the upstream flow of cold reactants into the recirculation zone. Moreover, their study explored the relationship between blowout and the stability of the shear layer, adding to the growing body of knowledge in this domain.

2 Theory

2.1 Combustion

Combustion is an exothermic chemical process in which an oxidizer reacts with a fuel, resulting in the release of energy in the form of heat and light. This process relies on several factors: the molecular-level mixing of fuel and oxidizer, the supply of sufficient heat to activate the reaction, and the necessary time for the reaction to progress. These chemical reactions initiate with the decomposition of reactants, leading to the creation of various species, as seen in the following reactions:

$$O_2 + H_2 \rightarrow H + HO_2 \tag{2.1}$$

$$2HO_2 \rightarrow H_2O_2 + O_2 \tag{2.2}$$

These reactions propagate through numerous intermediate species before culminating in the formation of product species, effectively terminating further reactions. Depending on the specific species involved, distinct *reaction chains* may occur. These chains persist until the initiation of radical chain reactions, which involve species with unpaired electrons.

Radical chain reactions, driven by free radicals, play a pivotal role in both igniting and sustaining the combustion process. For instance, the OH radical is instrumental in combustion initiation as it can react with fuel molecules to produce intermediate species capable of further reactions. Radical chain reactions also contribute to combustion propagation by generating intermediate species that interact with each other to form more stable products. This phenomenon, known as chain branching, is essential for sustaining the combustion process.

In the context of a stable flame, the chemical reactions responsible for heat release require a certain temperature threshold to continue until a stable product with no further heat release is achieved. These reactions occur primarily within a confined region known as the flame front, characterized by steep temperature and species concentration gradients. The thickness of the flame front is influenced by the time it takes for these reactions to occur.

Each reaction within this process has an associated reaction rate, which dictates the speed of reactant consumption and product formation. The reaction rate is significantly influenced by temperature, as described by the Arrhenius Law:

$$k_r = AT^b \exp\left(-\frac{E_a}{RT}\right) \tag{2.3}$$

Here, k_r is the reaction constant, T is the temperature, E_a is the activation energy, R is the universal gas constant, and A and b are constants. The exact values for these variables are given through the *reaction mechanisms*, which are data sets for the kinetics of reactions and thermophysical data for species.

Furthermore, the rate laws governing these reactions account for the abundance of reactants, indicating that the availability of reactants affects the production of species. In a reaction chain, one reaction usually acts as the rate-controlling step, dictating the overall reaction rate of the chain.

The effectiveness of combustion can be influenced by the degree of mixing between fuel and oxidizer, which can be enhanced by the flow field. Combustion can occur in two primary modes: laminar and turbulent. In laminar flames, diffusion is the primary mode of species transport, limiting reactant supply and overall heat release rate. These flames exhibit smooth, flat, and stable flame fronts, restricting the area available for reactions. In contrast, turbulent flames benefit from enhanced mixing, leading to increased reactant supply and heat release rates. Turbulence also distorts the flame front, creating a larger reaction volume.

The equivalence ratio, denoted as ϕ, is a crucial parameter for premixed reactants, representing the ratio of fuel to oxidizer (air) relative to the stoichiometric ratio:

$$\phi = \frac{m_{\text{fuel}}/m_{\text{air}}}{m_{\text{fuel, stoichiometric}}/m_{\text{air, stoichiometric}}}$$

A mixture is considered lean when ϕ is less than 1, indicating a fuel deficit, and rich when ϕ is greater than 1, indicating a fuel excess. The equivalence ratio significantly impacts heat release, combustion temperature, emissions, and flame stability.

2.2 Governing Equations

At a molecular level, fluids consists of relatively free-moving molecules that interact with each other physically, and, as described in sec. 2.1, chemically. The time and lengths scales that fluid motion occur at are much bigger than the molecular time and length scales, and so, as a simplification, fluid mechanics treats fluids as a continuum of matter. This allows for mathematically describing fluid behaviour using continuous functions. For this assumption to be valid, the conservation of mass must be respected, as described by eq. 2.4

$$\frac{\partial \rho}{\partial t} + \nabla \cdot (\rho \mathbf{u}) = 0 \tag{2.4}$$

Here, $\mathbf{u}$ is the local velocity vector.

The continuum assumption subjects the fluid to the conservation of momentum, as described by eq. (2.5)

$$\frac{\partial \rho \mathbf{u}}{\partial t} + \nabla \cdot (\rho \mathbf{u} \otimes \mathbf{u}) = -\nabla p + \nabla \cdot \boldsymbol{\tau} + \rho \mathbf{g} \tag{2.5}$$

Here, p is the local pressure, $\boldsymbol{\tau}$ is the viscous stress, and $\mathbf{g}$ is the gravitational acceleration vector. The viscous stress is expressed in its full term by eq. 2.6 [23]

$$\boldsymbol{\tau} = \left(2\mu \mathbf{D} - \frac{2}{3}\mu \left(\nabla \cdot \mathbf{u} \right) \mathbf{I} \right) \tag{2.6}$$

Here, $\mathbf{I}$ is the identity tensor, and $\mathbf{D} = \frac{1}{2}\left(\nabla \mathbf{u} + \nabla \mathbf{u}^T \right)$, known as the strain rate tensor. Conservation of internal energy e, potential energy p/ρ, and kinetic energy $\frac{1}{2}|\mathbf{u}|^2$ is described through the energy equation 2.7 [23].

$$\frac{\partial \rho h_0}{\partial t} + \nabla \cdot (\rho h_0 \mathbf{u}) = \frac{\partial p}{\partial t} + \nabla \cdot (\boldsymbol{\tau} \mathbf{u}) - \nabla \cdot \mathbf{q} + \rho \mathbf{g} \cdot \mathbf{u} + S_0 \tag{2.7}$$

Here, h_0 is the total energy, being $h_0 = e + p/\rho + \frac{1}{2}|\mathbf{u}|^2$, q is the heat flux, and S_0 is the source term, to account for energy stemming from chemical reactions or similar sources. Note that heat flux is often modeled as $q = \alpha \nabla h$, where $h = e + p/\rho$, and α being thermal diffusivity.

For chemically reactive flows, where chemical species can be consumed and produced by processes, species balance equation (2.8) must also be respected.

$$\frac{\partial \rho Y_i}{\partial t} + \nabla \cdot (\rho Y_i \mathbf{u}) = \nabla \cdot \mathbf{J}_i + \dot{\omega}_i \tag{2.8}$$

Here, $Y_i = \frac{m_i}{m}$, i.e the mass fraction of specie i in the mixture, $\mathbf{J}_i$ is the diffusive flux of specie i, and $\dot{\omega}_i$ is the source term of specie i, due to chemical reactions. Note that the source term is the net term, meaning that it accounts for both production and consumption of specie i. The diffusive flux $\mathbf{J}_i$ is often modeled by Fick's law 2.9, but this is a simplified diffusion model, which, as stated in the introduction of this thesis, fails to capture differential diffusion, counter-gradient diffusion, and other thermo-diffusive effects of low-Le reactants.

$$\mathbf{J}_i = -\frac{\rho \mathcal{D}}{M_i} \nabla Y_i \tag{2.9}$$

where $\mathcal{D}$ is the diffusion coefficient, and M_i is the molar mass of specie i.

2.2.1 Turbulence modeling

Turbulence is characterized by chaotic and dissipative eddies, that vary greatly in size. Turbulent motion affects the flow field and distribution and transport of scalars, and is hence

important to capture accurately to achieve representative CFD solutions - especially for combustion problems where specie transport is central. The size ratio between the smallest and largest length scales of turbulent eddies can be related to the Reynolds number Re of a flow, through the Kolmogorov length scale η [24]

$$\frac{\eta}{\ell_0} \propto Re^{-3/4} \tag{2.10}$$

where $_0$ is the integral length scale. As most real flows have Reynolds number in the thousands, if not millions, the length scales of turbulent motion spans over many order of magnitude. The distribution of turbulent kinetic energy across eddy sizes in the inertial subrange of turbulent flow scales with the wave number κ as

$$E(\kappa) \propto \kappa^{-5/3} \tag{2.11}$$

where $\kappa = \frac{2\pi}{\ell}$, where ℓ is the characteristic length of the eddy. This implies most of the turbulent energy is found in the largest eddies. To resolve all of these motions directly is computationally expensive because of this great span of length scales. As a compromise between feasibility and accuracy of CFD, large eddy simulation (LES) aims to resolve the scales where most of the energy is located, being the larger eddies, and model the smaller eddies. The cell size of a CFD simulation needs then to be sufficiently fine enough to capture the bigger eddies, but is allowed to be larger than the smaller, modeled eddies. This concept introduces the *sub-grid scale* (SGS), being the scales that is not captured by the mesh, and must hence be modeled.

Separation of the resolved scale and the sub-grid scale necessitates filtering each flow variable into a resolved and modeled component, that together represent the flow variable. A generic flow variable ϕ would then be represented as $\phi = \tilde{\phi} + \phi''$, where $\tilde{\phi}$ is the resolved component, and ϕ'' is the modeled component. Unlike Reynolds Averaged Navier-Stokes equations, the filtering happens spatially, not through time-averaging. To find the resolved component of a generic flow variable ϕ, a filtering operation through the filter function $G(\mathbf{x}, \mathbf{x}', \Delta)$ can be applied to the generic flow variable function $\phi(\mathbf{x}', t)$, as shown in eq. 2.12

$$\bar{\phi}(\mathbf{x}, t) = \int_{-\infty}^{\infty}\int_{-\infty}^{\infty}\int_{-\infty}^{\infty} G(\mathbf{x}, \mathbf{x}', \Delta)\, \phi(\mathbf{x}', t)\; dx_1'\, dx_2'\, dx_3' \tag{2.12}$$

where $\bar{\phi}(\mathbf{x}, t)$ is the filtered function, and Δ is the filter cut-off width. The filter cut-off has implications for the local cell size in the mesh. The cell size is often set so that the cube root of the cell volume is equal to Δ. By having the resolved component $\tilde{\phi}$ be Favre-averaged, i.e. $\tilde{\phi} = \dfrac{\overline{\rho\phi}}{\bar{\rho}}$, the filtered, unsteady Navier-Stokes equations for reactive flows (2.4 - 2.8) can be written as

$$
\begin{cases}
\dfrac{\partial \bar{\rho}}{\partial t} + \nabla \cdot (\bar{\rho}) = 0 & \text{(2.13aa)} \\
\dfrac{\partial \bar{\rho}\tilde{\mathbf{u}}}{\partial t} + \nabla \cdot (\bar{\rho}\tilde{\mathbf{u}} \otimes \tilde{\mathbf{u}}) = -\nabla \bar{p} + \nabla \cdot \bar{\boldsymbol{\tau}} + \bar{\rho}\mathbf{g} - \nabla \cdot \boldsymbol{\tau}_{SGS} & \text{(2.13ab)} \\
\dfrac{\partial \bar{\rho}\tilde{h_0}}{\partial t} + \nabla \cdot \left(\bar{\rho}\tilde{h_0}\tilde{\mathbf{u}}\right) = \dfrac{\partial \bar{p}}{\partial t} + \nabla \cdot (\bar{\boldsymbol{\tau}}\tilde{\mathbf{u}}) - \nabla \cdot \tilde{\mathbf{q}} + \bar{\rho}\mathbf{g} \cdot \tilde{\mathbf{u}} + S_0 - \nabla \cdot \mathbf{q}_{SGS} & \text{(2.13ac)} \\
\dfrac{\partial \bar{\rho}\tilde{Y_i}}{\partial t} + \nabla \cdot \left(\bar{\rho}\tilde{Y_i}\tilde{\mathbf{u}}\right) = \nabla \cdot \tilde{\mathbf{J}}_i + \overline{\dot{\omega}_i} - \nabla \cdot \mathbf{j}_i & \text{(2.13ad)}
\end{cases}
$$

Note that, in addition to the flow variables being Favre-averaged, new terms have appeared. The sub grid stress tensor $\boldsymbol{\tau}_{SGS}$, the sub grid energy flux $\mathbf{q}_{SGS}$, and the sub grid species mass fraction flux $\mathbf{j}_i$. Additionally, the the filtered total energy $\tilde{h_0}$ now is defined as $\tilde{h_0} = \tilde{e} + \bar{p}/\bar{\rho} + \frac{1}{2}|\tilde{\mathbf{u}}|^2 + k_{SGS}$, where k_{SGS} is the sub-grid turbulent kinetic energy. For LES, it is expected to have a grid fine enough such that at least the upper 80 % of the total turbulent kinetic energy cascade is being fully resolved. Total turbulent kinetic energy is then the sum of resolved turbulent kinetic energy $k_{resolved} = \frac{1}{2}\left(\overline{u_x'^2} + \overline{u_y'^2} + \overline{u_z'^2}\right)$ and k_{SGS}.

2.2.2 Subgrid scale modeling

The additional terms, $\boldsymbol{\tau}_{SGS}$, k_{SGS}, $\mathbf{q}_{SGS}$, and $\mathbf{j}_i$, needs to be solved through models. In LES, this is done through introducing a sub-grid viscosity, ν_{SGS}. There are many ways to model $\nu_{SGS]}$, but in the presented work, it is defined as

$$
\nu_{SGS} = C_k \Delta \sqrt{k_{SGS}} \tag{2.2}
$$

where C_k is constant. k_{sgs} is solved through the following its transport equation

$$
\frac{\partial \bar{\rho} k_{SGS}}{\partial t} + \nabla \cdot (\bar{\rho} k_{SGS} \tilde{\mathbf{u}}) = \nabla \cdot \left(\bar{\rho}\left(\bar{\nu} + \nu_{SGS}\right) \nabla k_{SGS}\right) + \bar{\rho} G - \frac{2}{3}\bar{\rho} k_{SGS} \nabla \cdot \tilde{\mathbf{u}} - \frac{C_e \bar{\rho} k_{SGS}^{3/2}}{\Delta} + S_k \tag{2.3}
$$

where G is the turbulent production term defined as

$$
G = 2\,\nu_{SGS}\left(\nabla \tilde{\mathbf{u}}\right)^T : \tilde{\mathbf{D}} \tag{2.4}
$$

With ν_{SGS} defined, equations 2.13ab, 2.13ac, and 2.13ad can finally be closed, with the following definitions.

$$
\boldsymbol{\tau}_{SGS} = 2\bar{\rho}\left(-\nu_{SGS}\left(\nabla \tilde{\mathbf{u}}\right)^T + \frac{1}{3} k_{SGS} \mathbf{I}\right) \tag{2.5}
$$

$$\mathbf{q}_{SGS} = -\bar{\rho}\frac{\nu_{SGS}}{Pr_{SGS}}\nabla\tilde{h_0} \tag{2.6}$$

$$\mathbf{j}_i = -\bar{\rho}\frac{\nu_{SGS}}{Sc_{SGS}}\nabla\tilde{Y_i} \tag{2.7}$$

Here, Pr_{SGS} and Sc_{SGS} is the turbulent Prandtl number and turbulent Schmidt number, respectivly. Pr_{SGS} is the ratio between the subgrid viscosity nad subgrid themral diffusivity. Sc_{SGS} is the ratio between subgrid viscosity and subgrid mass diffusivity.

2.3 Reaction modeling

In modeling turbulent reactive flows, such as combustion, a wide range of length and time scales must be considered. Some reactions may occur on very short time scales, on the order of 10^{-10} seconds [25], while large-scale motions in the flow can have time scales on the order of seconds. Additionally, chemical interactions take place at a much smaller length scale compared to the integral length scale of the flow. Managing this wide range of scales is computationally demanding, which necessitates the use of models to reduce computational costs. However, accurately modeling the non-linear relationship between chemical reactions and turbulence remains a significant challenge.

For certain applications, it is reasonable to assume that the reaction time scale is negligible compared to the flow time scales. This assumption implies that the reaction between fuel and oxidizer instantaneously produces product species upon contact, a concept known as *infinitely fast chemistry*. Nevertheless, intermediate species and their distribution can exert a considerable influence on energy release and product species formation. As previously discussed [**?**], certain intermediate species can serve as rate-controlling factors. Therefore, the formation and consumption rates of intermediate species must be explicitly considered, as is done in the finite rate chemistry model. While the desire is to include as many intermediate species and reactions as possible, the impact of some species is more significant than others. Consequently, some species and reactions can be disregarded, leading to reduced mechanisms that focus solely on the influential reactions and species. These reduced mechanisms encompass tabulated data for the constants used in the Arrhenius equation 2.3 and thermodynamic information for each species. Despite being referred to as "reduced," these mechanisms can still cover a substantial array of species and reactions. For methane-air combustion, the widely used GRI-Mech 3.0 [26] includes 53 species and 325 reactions.

To account for turbulence-chemistry interactions, a flame element can be treated as an open reactor, which can be divided into two components: a reacting fraction, where chemical reac-

tions occur, and a non-reacting fraction, where species mixing occurs [27]. The Partially Stirred Reactor model (PaSR) developed by Chomiak and Karlsson [28] posits that the reaction rate in a reactor depends on the mass exchange between these reactive and non-reactive fractions, as expressed in equation 2.8:

$$\frac{\bar{\rho}}{\tau^R}\left(Y_i^R - Y_i^N\right) = \dot{\omega}_i^R\left(\bar{\rho}, T^R, Y_i^R\right) \tag{2.8}$$

In this equation, $\bar{\rho}$ represents the Reynolds-averaged density in the cell, τ^R is the residence time in the reactive fraction, $\dot{\omega}_i^R$ denotes the production rate term described in equation 2.8, T^R signifies the temperature in the reactive fraction, and Y_i^R and Y_i^N are the mass fractions of specie i in the reacting and non-reacting fractions, respectively.

Given the assumption that chemical reactions occur only in the reacting fraction, the total production rate for specie i within the cell can be formulated as shown in Equation 2.9:

$$\overline{\dot{\omega}_i} = \kappa\dot{\omega}_i^R = \kappa\frac{\bar{\rho}\left(Y_i^R - Y_i^N\right)}{\tau^R} \tag{2.9}$$

In this equation, $\overline{\dot{\omega}_i}$ represents the production rate of specie i for the entire cell. The reacting fraction is modeled as a perfectly stirred reactor.

The parameter κ is determined by the relationship shown in equation 2.10:

$$\kappa = \frac{\tau_{chem}}{\tau_{chem} + \tau_{mix}} \tag{2.10}$$

Here, τ_{chem} denotes the chemical time scale, and τ_{mix} represents the mixing time scale. κ ranges between zero and one, as values beyond this range would imply unphysical negative time scales. A common approach is to use a turbulent time scale τ_{turb} as the mixing time scale τ_{mix}. Chomiak suggested defining τ_{mix} based on turbulent values, as shown in equation 2.11:

$$\tau_{turb} = \sqrt{\frac{k}{\epsilon}\left(\frac{\nu}{\epsilon}\right)^{\frac{1}{2}}} \tag{2.11}$$

Conversely, τ_{chem} is defined based on the largest relative consumption rate of fuel or oxidizer, as depicted in equation 2.12:

$$\tau_{chem} = \rho\left(\max\{\frac{-\dot{\omega}_{Fuel}}{Y_{Fuel}}, \frac{-\dot{\omega}_{Ox}}{Y_{Ox}}\}\right)^{-1} \tag{2.12}$$

This approach ensures that the reactant depleted first becomes the limiting reactant, dictating the chemical time scale. Comparisons conducted in [27] indicate that Chomiak's τ_{chem} provides good results for major species but underperforms in predicting intermediate species.

3 Method

3.1 Case overview

This thesis aims to replicate both the M1 and A1 flame of Wiseman [2]. The fuel mix of M1 is 100 vol-% CH_4. The fuel mix of A1 is 40 vol-% NH_3, 45 vol-% H_2, 45 vol-% N_2. Both flames have $\phi = 0.6$, and are premixed with air. The main metric of interest in the simulation is at which $\mathbf{u}_{\text{lip}}$ the blow-out event start at. For the M1 flame, the experiment reported $\mathbf{u}_{\text{lip}=12m/s}$. For the A1 flame, $\mathbf{u}_{\text{lip}=120m/s}$. Combustion products and other emissions are not of interest for this thesis.

3.2 Solver

The CFD simulations in this thesis were conducted using the open-source CFD toolbox known as `OpenFOAM` [29]. `OpenFOAM` is a versatile software package that provides a wide array of specialized numerical solvers and pre/post-processing tools tailored for solving problems in continuum mechanics, particularly in the field of CFD.

From the `OpenFOAM` library of solvers, the pressure-based `multicomponentFluid` [30] was employed. This solver is designed to solve unsteady, compressible, turbulent flows with heat transfer and reactivity, such as combustion processes.

The `multicomponentFluid` solver employs the PIMPLE algorithm for the coupling of pressure and velocity. The PIMPLE algorithm is a combination of the transient PISO and steady-state SIMPLE algorithms [23]. Briefly explained, the PIMPLE algorithm treats each time step as a steady-state problem, solved with the SIMPLE algorithm, and transitions between time steps with the PISO algorithm.

The PIMPLE algorithm in `OpenFOAM` allows for adaptive time-stepping, which enables adapting the time step according to the Courant–Friedrichs–Lewy condition given in equation 3.1

$$C = \frac{u_x \Delta t}{\Delta x} + \frac{u_y \Delta t}{\Delta y} + \frac{u_z \Delta t}{\Delta z} \leq C_{max} \tag{3.1}$$

C_{max} was set to 0.8 in this simulation, for which a resulting Δt is calculated. No reduction in Δt due to chemical reactions was observed, although a sufficiently rigorous data analysis was not performed to guarantee this.

3.2.1 Schemes

The schemes are summarized in table 1. The schemes are first-order in time and second-order and bounded in space.

Table 1. Summary of numerical schemes.

Time integration	`Euler`
Gradient ∇	`cellLimited Gauss linear`
Divergence $\nabla\cdot$	`Gauss linearUpwind`
Laplacian ∇^2	`Gauss linear limited 0.777`
Interpolation	`linear`
Surface normal gradient	`limited 0.777`

For solving the chemistry, an implicit Euler method was used, with an initial timestep of $\Delta t_{chem} = 1 \cdot 10^{-7} s$

3.2.2 Convergence

The simulation successfully converged to the chosen criteria of $1 \cdot 10^{-7}$ for pressure and $1 \cdot 10^{-8}$ for the other terms during the simulation. Two outer loops were performed, with one non-orthogonal corrector loop for each time step.

3.3 Models

3.3.1 Molecular transport

The `OpenFOAM` version used in this thesis employs a fickian diffusion model 3.2 by default.

$$\mathbf{J} = -\rho D_{m,i} \nabla Y_i \tag{3.2}$$

where ρ is the density of the mixture, and $D_{m,i}$ is the mixture-averaged cofficient, given by

$$D_{m,i} = \frac{1 - Y_i}{\sum_{j \neq i} K \frac{X_j}{\mathcal{D}_{ji}}} \tag{3.3}$$

3.3.2 Turbulence

As presented in sec. 2, LES was employed for resolving turbulence. For sub-grid scale modeling, the `dynamicKEqn`[31] model was used, in combination with `simple` filter.

3.3.3 Thermopysical properties

For modeling temperature dependency of viscosity, the standard Sutherland model [30] was employed.

$$\mu = \frac{A_s\sqrt{T}}{1 + T_s T^{-1}} \tag{3.4}$$

where A_s and T_s are coefficients.

The JANAF tables were used to find the mixture's heat capacity c_p and enthalpy H. As shown in eq 3.5, the JANAF table [32] is interpolated by the NASA polynomials.

$$\begin{aligned} \frac{C_p}{R} &= a_1 + a_2 T + a_3 T^2 + a_4 T^3 + a_5 T^4 \\ \frac{H}{R} &= a_1 T + \frac{a_2 T^2}{2} + \frac{a_3 T^3}{3} + \frac{a_4 T^4}{4} + \frac{a_5 T^5}{5} + a_6 \end{aligned} \tag{3.5}$$

For solving the equation of state, ideal gas was assumed, giving the following equation

$$\rho = \frac{p}{RT} \tag{3.6}$$

3.3.4 Radiation

Radiation was neglected. Radiation is a form of heat loss significant for rich flames producing soot and emitting species, like CO_2 [33]. None of the falmes simulated produced soot, and the mass fraction of CO_2 in the product composition for the CH_4-air flame is relatively small. As such, it is assumed that the radiation loss has negligible influence on the current problem.

3.3.5 Reaction model

For the simulation, the already explained PaSR-model was used, with a `Rosenbrock34` ODE-solver to solve the balance matrix.

3.3.6 Reaction mechanism

Three different data sets were used for reaction modeling. For the CH_4-air flame, The reaction mechanism by Lu and Law was used [34], from here on referred to as the Lu mechanism. For the $NH_3/H_2/N_2$-air flame, both the San Diego mechanism by Yiang et al. (2020) [35] and the Vargas mechanism by Vargas et al. (2024) [36]. The reaction mechanism is summarized in table 2.

These three reaction mechanism were compared to each other in Cantera, which is an open-source suite of tools for problems involving chemical kinetics, thermodynamics, and transport processes [37]. The mixtures were setup using a as a freely propagating one-dimensional flame

Table 2. Summary of reaction mechanisms.

Mechanism	GRI-Mech 3.0	Lu	San Diego	Vargas
Elements considered	H, C, N, O	H, C, N, O	H, N, O	H, N, O
Number of species	53	30	19	22
Number of reactions	325	184	60	120

at $p = 1atm$, with reactants temperature being $T = 300K$. The resulting laminar flame speed, $S_{L,0}$, adiabatic flame temperature, T_{ad}, and flame thickness, δ_{ad}, are compared in table **??** against the well-known GRI-Mech 3.0 mechanism [26].

The detailed Lu mechanism is derived from the more comprehensive GRI-Mech 3.0 mechanism. While GRI-Mech 3.0 accounts for 53 species and 325 reactions, the Lu mechanism accounts for 30 species and 184 reactions. This reduction in size of the mechanism provides significant savings in computational time per time step, but yet manages to capture the quantitative behaviour of a lean CH_4-air flame, as seen in table 3. This is in-line with the developers reporting [38]. Hence, it was deemed unnecessary to perform a CFD run with the GRI-Mech 3.0 mechanism. The altered San Diego mechanism is developed for gas turbine application, under the assumption that the reactants are preheated to a temperature of 600-800 K, and that the combustion process takes place at elevated pressures. As reported by the developers of the mechanism, this assumption leads to underprediction of laminar flame properties at atmospheric pressure and room temperature. The mechanism accounts for 19 species and 60 reactions. The slightly bigger Vargas mechanism accounts for 22 species and 120 reactions, and is developed for more general applications. The Vargas mechanism predicts higher laminar flame speed and lower flame thickness than the San Diego mechanism, by a relative difference of 19 % and 15 % respectively. The GRI-Mech 3.0 mechanism, which is developed for CH_4-air combustion, predicts lower laminar flame speed, higher flame thickness, and slightly cooler flame temperature. As the mechanism was not developed for ammonia-combustion, this discrepancy in predicted values compared to the mechanisms designed for ammonia-combustion is not of surprise, but shows that larger mechanisms does not guarantee better accuracy. The GRI-Mech 3.0 mechanism was deemed irrelevant for CFD simulating, and included in table **??** only to provide a reference point for the Lu, San Diego and Vargas mechanisms, to highlight the importance of using mechanisms developed for ammonia combustion.

To evaluate how well the mechanism predicts the total heat release rate, the total heat release rate will be compared against the *theoretical* total heat release rate $\widehat{HRR}_{tot}$ which is

Table 3. Summary of laminar flame properties as predicted by Cantera.

Mixture	CH_4		$NH_3/H_2/N_2$		
Mechanism	GRI-Mech 3.0	Lu	GRI-Mech 3.0	San Diego	Vargas
$S_{L,0}$ $[ms^{-1}]$	11.58	11.63	7.46	12.45	15.35
T_{ad} $[K]$	1664	1664	1622	1635	1630
δ_{ad} $[mm]$	0.980	0.977	1.871	1.016	0.847

CH_4	$50 \cdot 10^6$
NH_3	$18.8 \cdot 10^6$
H_2	$120 \cdot 10^6$

Table 4. Lower Heating Value for fuels

defined as

$$\widehat{HRR}_{tot} = \rho \sum_i Y_i \mathrm{LHV}_i \tag{3.7}$$

where LHV_i is the lower heating value of reactant i, as seen in table **??**. The data is retrieved from the NIST Standard Reference Database [3]. This gives a crude approximation of the maximum total heat release rate for the flame, given that all the reactants are burnt. $\widehat{HRR}_{tot}$ will be used to judge the effectiveness of the burn rate for a mechanisms.

3.4 Domain

The problem domain was modeled after Wiesman's experimental setup [2], as illustrated in figure 2. The domain is axisymmetric 3D. The distance between the top of the bluff body and the inlet is $20mm$. The diameter of the domain after the bluff body is $100mm$, and extends $100mm$ height wise above the bluff body. In terms of bluff body diameters D_{BB}, the domain measures $7.7D_{BB}$ wide and $7.7D_{BB}$ high. In Wisemans experiment, the diameter of the dump plane around the bluff body is $150mm$, which is larger than the computational domain. It is assumed that the relatively smaller computational domain should not affect the result. It's worth noting that a formal sensitivity analysis of the domain size was not conducted.

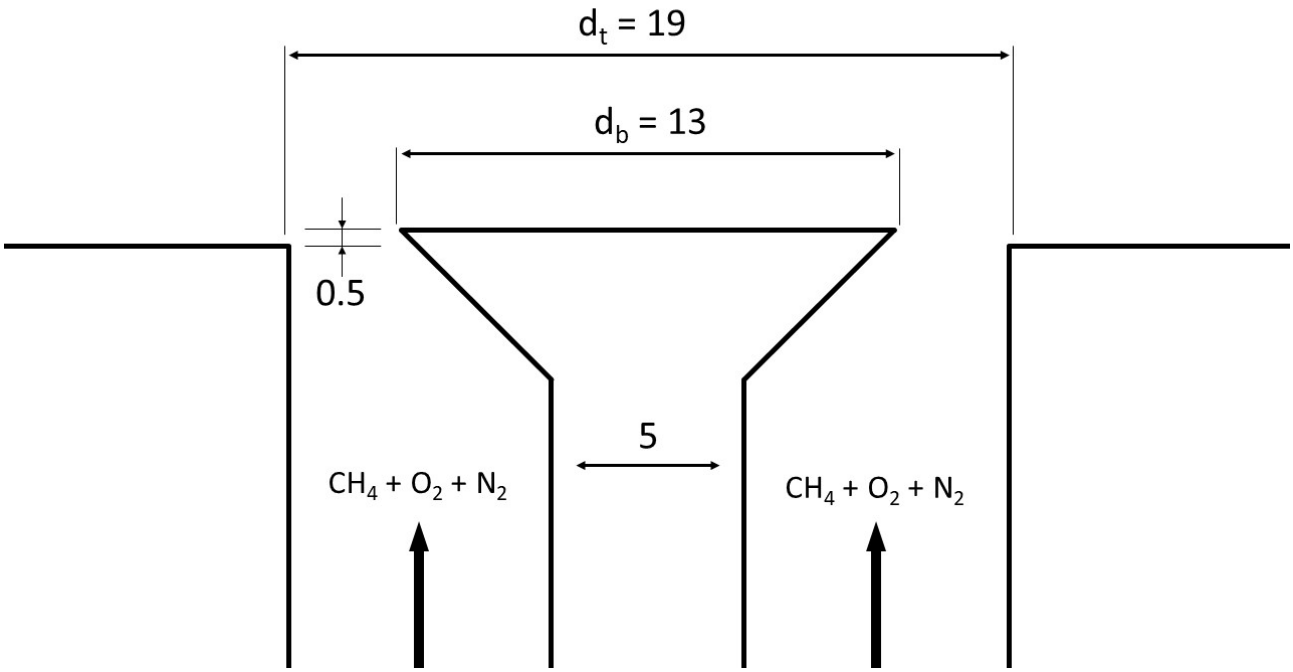

Figure 2. Schematic of the bluff body. All measurements are in millimeter.

3.4.1 Mesh

The mesh was generated using the `blockMesh` utility in `OpenFOAM v2306`. This alternative version of `OpenFOAM` was used due to compatibility problems with the inline calculation utility. After production of the mesh, it was move to a `OpenFOAM v11` case. The mesh was fully 3D OH-type grid, consisting of 6,004,821 non-uniform hexahedral cells. Cells in the recirculation zone were smaller, and had the target cell length of $240\mu m$. This cell length should provide about 4 cells throughout the flame front. Some cells were smaller due to transitions between geometries. Cell quality, found through the utility `checkMesh`, was sufficient. The summary of

the cell quality can be found in table 5 It was verified that the mesh did resolve 80 % of the turbulent kinetic energy in the area of interest, being the high-temperature areas. The inlet, immediate area around the lip of the bluff-body, and the zone near the outlet of the domain resolved less than 80% of the turbulent kinetic energy. Implications of this will be discussed later in section **??**.

Table 5. Summary of cell quality of the mesh, as reported by `checkMesh`.

Metric	Value
Max aspect ratio	53.98
Max mesh non-orthogonality (average)	44.01 (2.90)
Max skewness	1.08

A non-reactive simulation with target cell size of $100\mu m$ was ran, to gage cell size influence on the flow field.

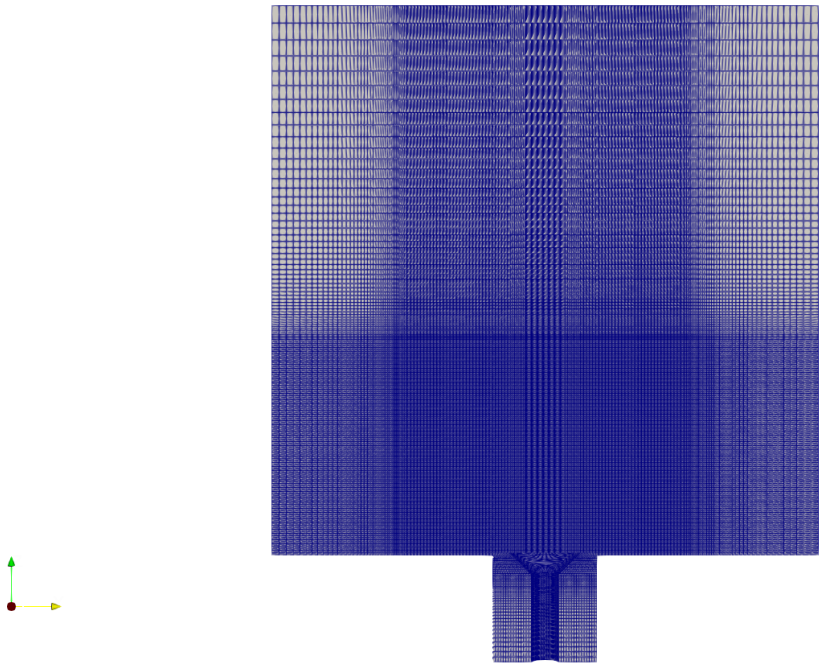

Figure 3. Picture of the mesh used.

3.4.2 Initial and Boundary Conditions

The boundary conditions are summarized in table 6. Each function and setting will be explained in more depth after the table. In the table, `TIKEI` are shorthand for `turbulentIntensityKineticEnergyInlet`.

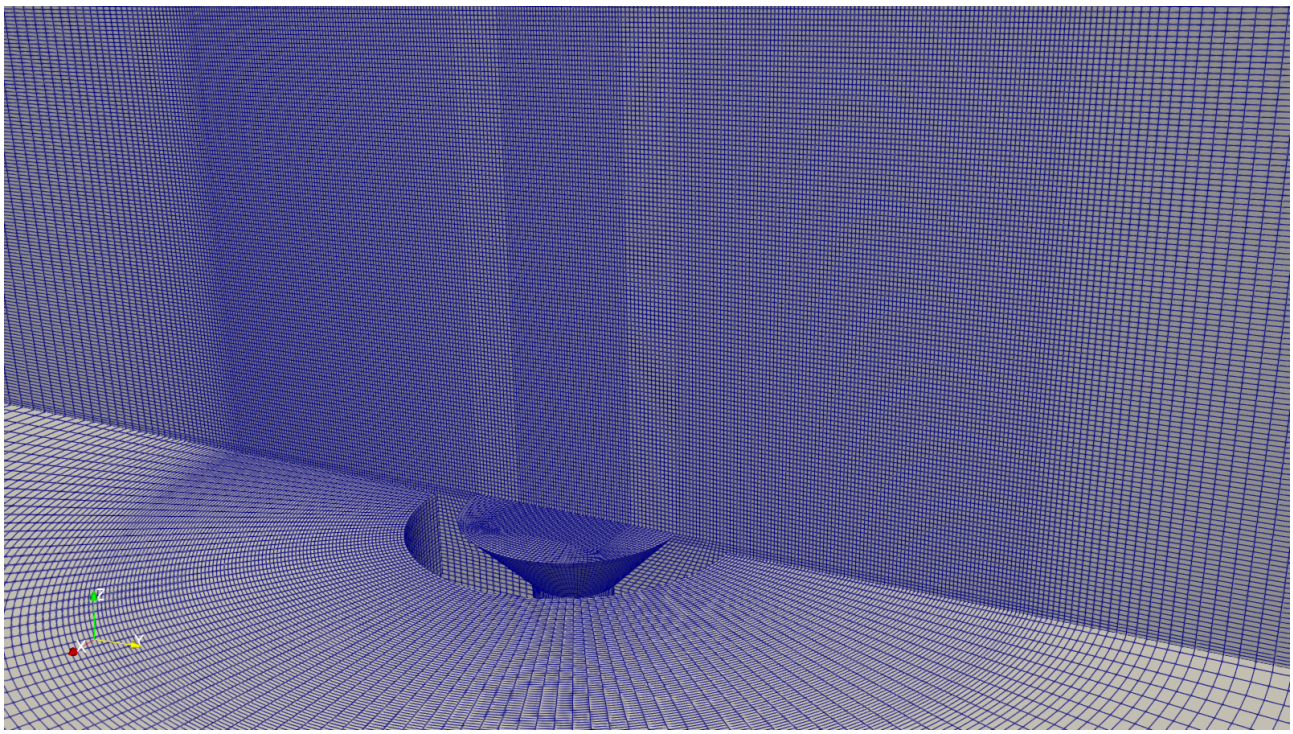

Figure 4. Detail picture of the mesh around the bluff body.

For velocity **U**, the inlet velocity was varied during the simulation. The strategy was to increase the inlet velocity $\mathbf{u}_{\text{in}} over a period of 1 ms and let the flame stabilize before another increase in velocity occ$ *slip is applied at all solid surfaces. For the outlet,* `waveTransmissive` *condition was chosen. The* `waveTransmis` *reflective for waves*[39].

For pressure p, the inlet condition is `fixedFluxPressure`, which adapts the pressure gradient to fulfill the flux condition on the same patch set by the inlet velocity condition. For the outlet, `waveTransmissive` condition was chosen.

For temperature T, the inlet flow was set to $T = 301K$. For simplification, the same fixed value was imposed on all solid surfaces.

For the species Y_i, zero-gradient was applied at all solid surfaces and outlets. Only the inlet patch had a specified composition, being premixed reactants with equivalence ratio $\phi = 0.6$, leading to a composition of $Y_{N_2} = 0.741$, $Y_{O_2} = 0.230$, and $Y_{CH_4} = 0.0338$ for the CH_4-air flame. The $NH_3/H_2/N_2$-air case was defined with $Y_{N_2} = 0.729$, $Y_{O_2} = 0.211$, $Y_{NH_3} = 0.0515$, and $Y_{H_2} = 0.00686$.

fort the turbulent kinetic energy k, zero-gradient was applied to the outlet. For the inlet, the `turbulentIntensityKineticEnergyInlet` condition was applied, which calculates k based on user-specified turbulence intensity I, using equation 3.8. It was assumed that the flow was moderately turbulent, so $I = 0.1$ was set. At all solid surfaces, the `kqRWallFunction` wall model were employed for k.

Table 6. Summary of boundary conditions.

	Inlet	Outlet	Solid surfaces
Velocity	`uniform FixedValue`	`waveTransmissive`	`noSlip`
Pressure	`fixedFluxPressure`	`waveTransmissive`	`zeroGradient`
Temperature	`fixedValue`	`zeroGradient`	`fixedValue`
Species	`fixedValue`	`zeroGradient`	`zeroGradient`
k	`TIKEI`	`zeroGradient`	`kqRWallFunction`
α_t	`calculated`	`calculated`	`compressible::alphatWallFunction`
ν_t	`calculated`	`calculated`	`nutkWallFunction`

$$k = 1.5(I|U|)^2 \tag{3.8}$$

This study used an already-developed flame as the initial condition for all fields. The initial flame had $\mathbf{u}_{\text{lip}} = 5.7ms^{-1}$. The simulation for the initial flame was run from ignition until an approximately stable state was achieved.

4 Validation & Verification

4.1 Validation

Due to errors in numerical methods, it is important to verify that the chosen models and methods are correctly implemented. The PaSR model will be assessed first. The model has been tested numerous times [40],[41],[27], and the current choice for modeling τ_{chem} and τ_{mix} is reported to reproduce product concentrations quite well. The mechanism developed by Lu and Law has been tested against more comprehensive mechanisms and manages to reproduce the solution of the more advanced mechanisms quite well for the equivalence ratio ϕ used in this simulation [38]. The San Diego mechanism is developed for gas turbine simulations, where the reactant temperature is significantly elevated, and the combustion process takes place under higher pressures. Hence, this set is applied to a situation that the developers [35] of the mechanism consider an edge case. Based on this, it is believed that the choice to use PaSR is appropriate, and its implementation is correct. The anticipated temperature range is well within the working range of the thermophysical models.

As required in LES, over 80 % of the turbulent kinetic energy was resolved in the area of interest, as can be seen in fig. 5.

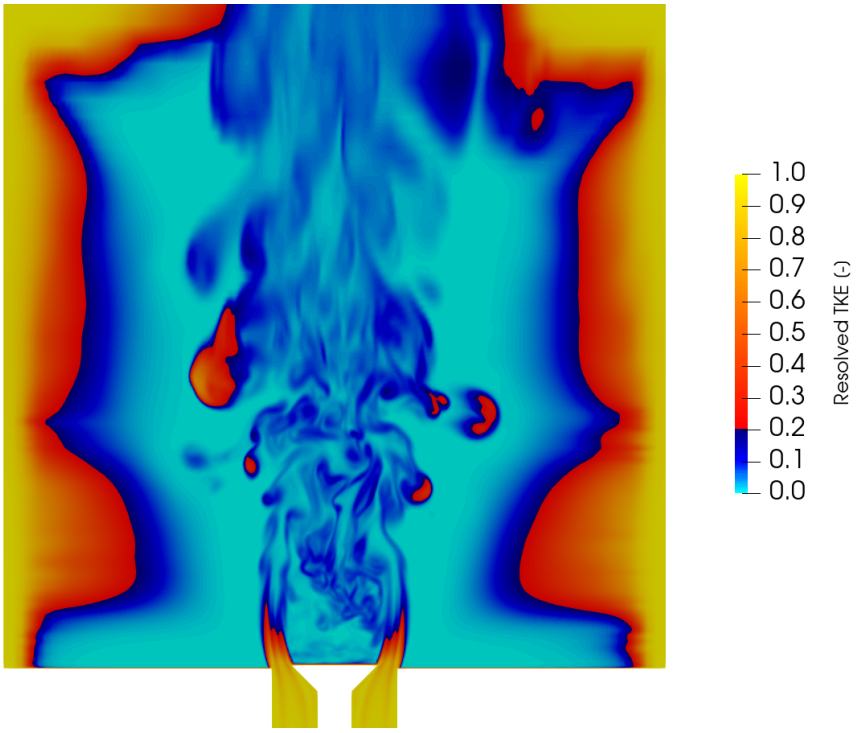

Figure 5. Plot of the ratio of total turbulent kinetic energy that is resolved. Any area with value below 0.2 fulfills the LES requirement to the mesh.

To see whether the flow field would be affected by having smaller cells, the simulation setup

was run on a mesh with a target cell length of 100 μ m. The radial velocity magnitude profile between the mesh used for blow-out simulation, having cell target cell length 240 μ m, at two different heights; at the bluff-body plane, and at one $\frac{1}{2}$ of D_{BB} above the bluff-body plane. The two solutions can be seen in fig. 6. As can be seen, the difference between the two meshes is negligble, and hence the original cell length of 240 μ m was deemed fine enough.

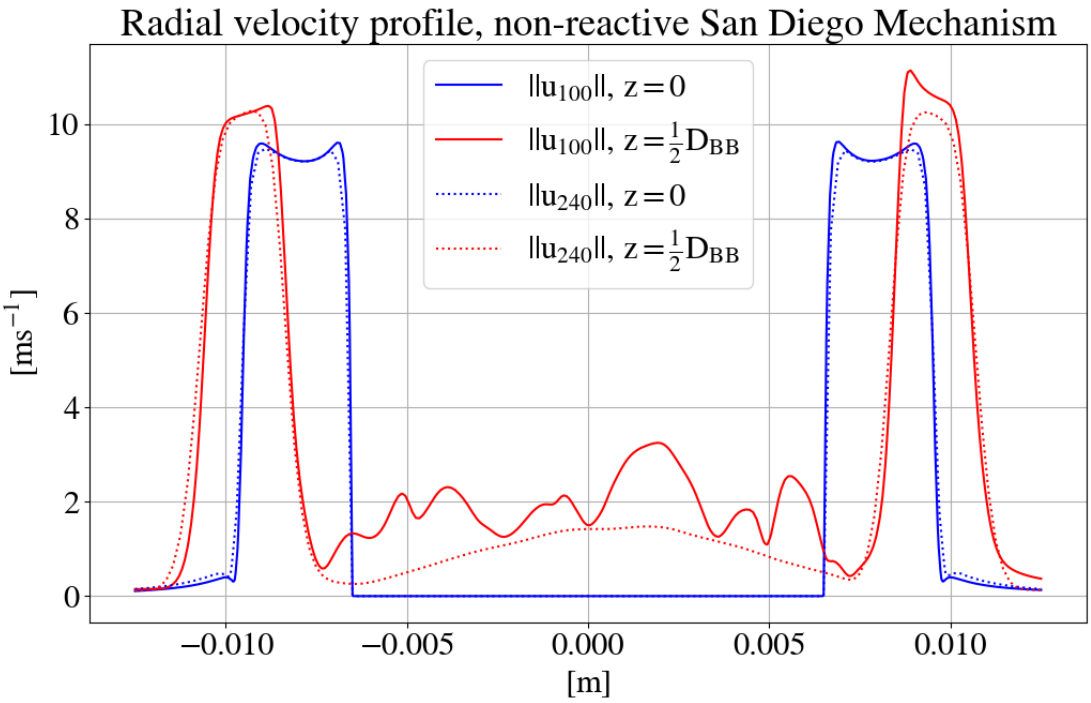

Figure 6. Radial profile of velocity magnitude for mesh with cell length 100 μm, and 240 μm.

4.2 Verification

The simulation is directly modeled after Wisemans experiment [2]. This provides an excellent point of comparison. The limitation of the comparison is the lack of absolute values of specie distribution, and so the point of comparison beyond $\mathbf{u}_{\text{lip}}$ becomes very qualitative. Because of this, comparison to Canteras laminar flame is made where appropriate. Still, the goal of this project is to simply assess if blow-out at the correct $\mathbf{u}_{\text{lip}}$ can be reproduced by the presented model.

5 Results

A summary of key results can be found in table 7

Table 7. Summary of CFD results. All values are at blow-out.

Mixture	CH_4	$NH_3/H_2/N_2$	
Mechanism	Lu	San Diego	Vargas
Numerical $\mathbf{u}_{\text{lip}}$ $[ms^{-1}]$	10.8	12.6	18.0
Experimental $\mathbf{u}_{\text{lip}}$ $[ms^{-1}]$	12	120	120
Numerical Re [-]	12827	13900	19858

As can be seen in the table, the CH_4 flame achieved close to experimental $\mathbf{u}_{\text{lip}}$, underestimated by 10 %. The $NH_3/H_2/N_2$ flame significantly underpredicted $\mathbf{u}_{\text{lip}}$ by an order of magnitude with both mechanisms, relative to experiment. Each case will be presented in its own section.

5.1 CH_4 with Lu mechanism

The numerical CH_4-air flame will be presented first.

The peak HRR_{tot} was found to be approximately 11.5 ms in Fig. 7. Note that the HRR_{tot} is very stable during the simulation, even during increases of $\mathbf{u}_{\text{lip}}$. HRR_{tot} is relatively low compared to $\widehat{HRR}_{tot}$. Before the increase in speed, the numerical HRR_{tot} was only 45 % of $\widehat{HRR}_{tot}$. The first increase in velocity to $\mathbf{u}_{\text{lip}} = 9m/s$ does not significantly change HRR_{tot}. The relative error between $\widehat{HRR}_{tot}$ and HRR_{tot} is now 62 %. Neither the second velocity increase to $\mathbf{u}_{\text{lip}} = 10.8m/s$ does much for HRR_{tot}. By the time the next velocity increase occurs, HRR_{tot} has already fallen below 50 % of its maximum value, indicating that the third velocity increase did not affect when the extinction occurred.

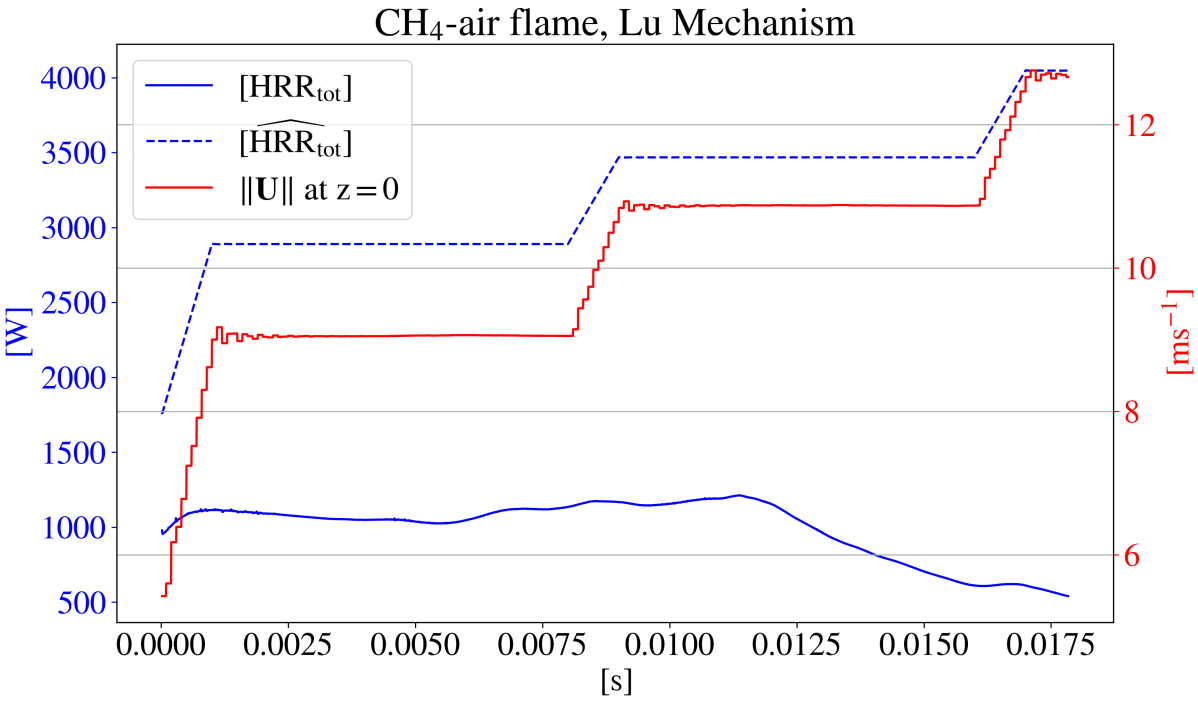

Figure 7. HRR_{tot} and $\mathbf{u}_{lip}$ over time

5.1.1 Flame front

5.1.2 Transient behaviour

The immediate first 10 ms after peak HRR_{tot} was achieved is visualized for fields of interest in Figs. 8 and 9.

Table 8. Peak values of CH_4-air flame, compared to laminar values predicted by Cantera.

Qunatity	Y_{CH_4} [-]	T [K]	HRR [w/m^3]	Y_{OH} [-]	Y_{CO} [-]
CFD	$33.8 \cdot 10^{-3}$	1651	$0.824 \cdot 10^{9}$	$1.46 \cdot 10^{-3}$	$18.91 \cdot 10^{-3}$
Cantera	$33.8 \cdot 10^{-3}$	1665	$0.568 \cdot 10^{9}$	$1.39 \cdot 10^{-3}$	$16.43 \cdot 10^{-3}$

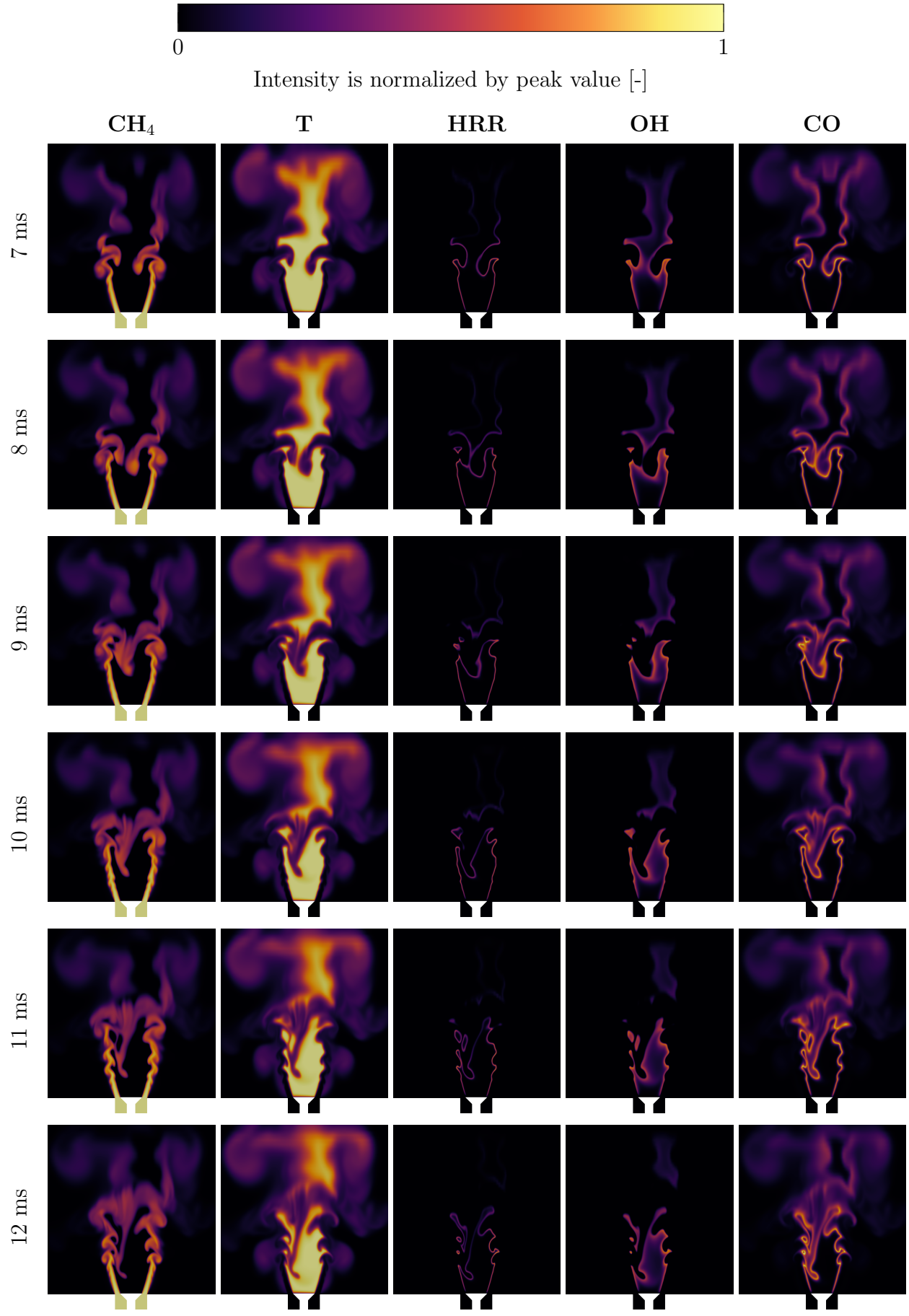

Figure 8. Time-series of instantaneous fields over different time intervals using the Lu mechanism.

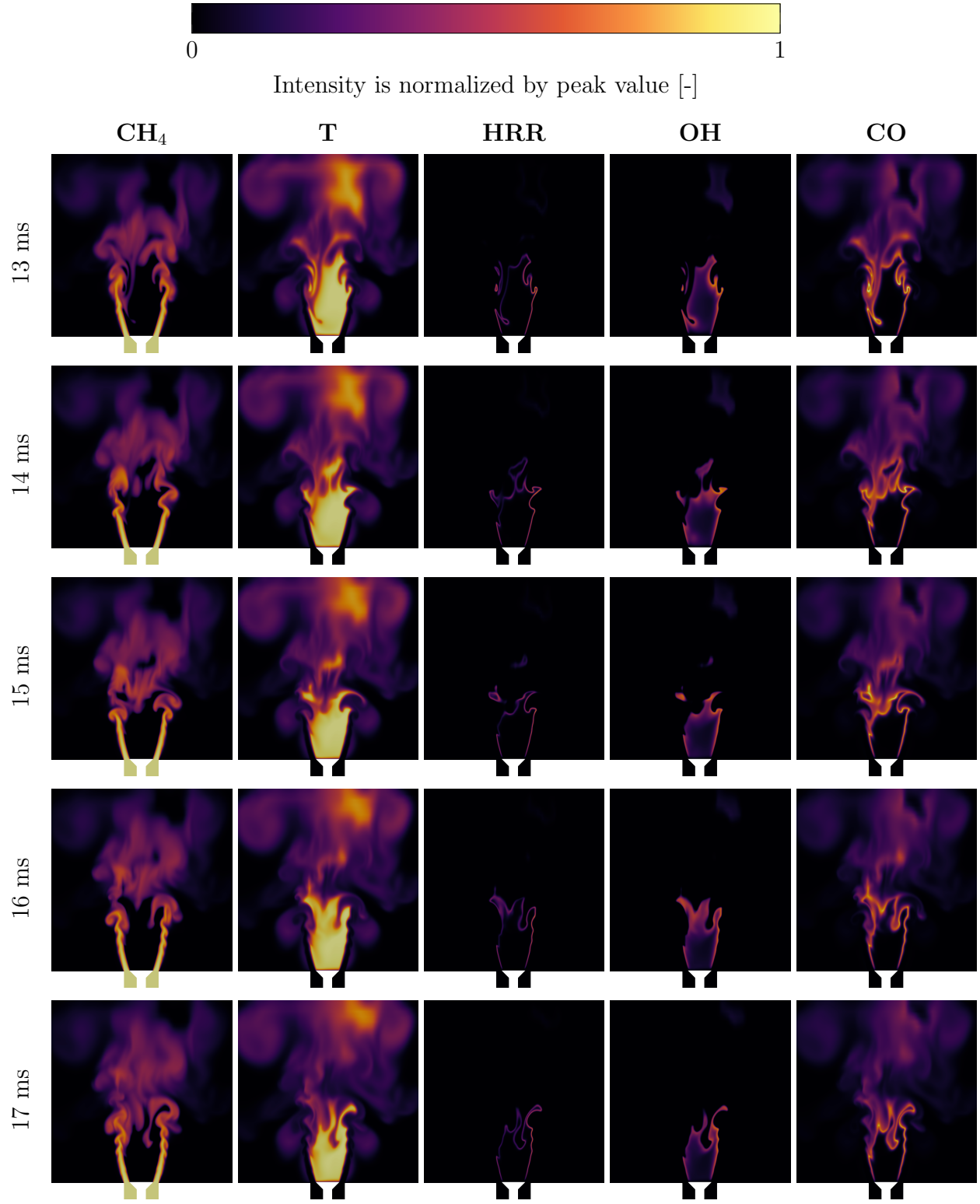

Figure 9. Time-series of instantaneous fields over different time intervals using the Lu mechanism.

For some distance downstream immediately after the bluff body, the reactant stream maintains a smooth, uncontorted, straight, jet-like appearance. At 2 D_{BB} downstream, the reactant flow becomes turbulent, generating eddies. These eddies diffuse the CH_4 concentration throughout the downstream domain of the recirculation zone. The eddies vary in size over time and with the distance at which they appear.

The CH_4 distribution indicates that unburnt reactants are drawn into the core of the recirculation zone just after the crest of the recirculation zone. Between timestamps 8 ms and 12 ms, a column of CH_4 with a lower concentration penetrates deep into the recirculation zone, rapidly moving towards the bluff body. However, this column is pushed aside before being fully consumed. As time progresses, the crest of the recirculation zone moves closer to the bluff body, and in later time steps, the CH_4 entering the core appears to be in lower concentration.

Almost the entire recirculation zone appears to be near its peak temperature. However, as the cold reactants enter the core, the recirculation zone appears to locally cool down. The high-temperature zone also seems to shrink with time.

The HRR (heat release rate) appears to be uniformly distributed along the flame front. Local curvature in the flame front does not significantly affect the HRR. The HRR sheet crinkles and deforms noticeably. As early as timestamp 8 ms, there are disconnected "islands" of significant HRR values. The side of the flame that sheds these islands appears to reduce local HRR over time.

The OH distribution appears to be entirely encapsulated by the HRR sheet and closely follows its surface. The surface of the OH volume appears smooth and closely resembles the instantaneous OH imaging in the Wisemans experiment. The OH volume seems to be approximately twice as tall as the experimental distribution.

CO, as an end product and not an intermediate species, appears to be generated at a higher rate when CH_4 is present in the core of the recirculation zone. It is worth noting that areas with high CO concentrations correlate well with areas of lower HRR in the flame front.

5.2 Vargas

The numerical $NH_4/H_2/N_2$-air flame simulated with the Vargas mechanism will be presented.

The peak HRR_{tot} was found just after 10 ms in Fig. 10. Before the first velocity increase, the HRR_{tot} quite close to $\widehat{HRR}_{tot}$, with only 7 % realtive difference. After the first increase in velocity to $||\mathbf{u}||_{lip} = 11m/s$, HRR_{tot} exhibited large oscillations in values, but came within 3 % of $\widehat{HRR}_{tot}$ within the next velocity increase. After the next velocity increase to $||\mathbf{u}||_{lip} = 16m/s$, HRR_{tot} came within 1 % of $\widehat{HRR}_{tot}$, but falls quickly before returning to the approximately same value. The next velocity increase to $||\mathbf{u}||_{lip} = 18m/s$ trigger blow-out at 15.9 ms.

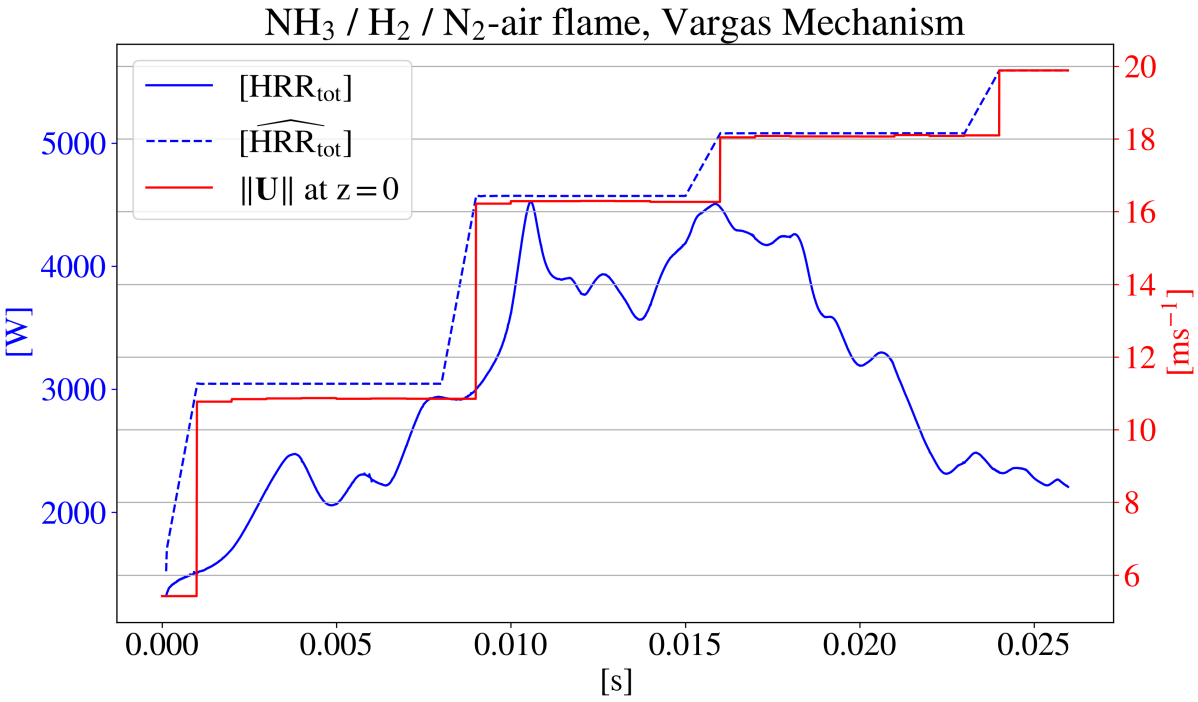

Figure 10. HRR_{tot} and $\mathbf{u}_{lip}$ over time

Table 9. Peak values of $NH_3/H_2/N_2$-air flame, compared to laminar values predicted by Cantera.

	Y_{NH_3} [-]	Y_{H_2} [-]	T [K]	HRR [w/m^3]	Y_{OH} [-]
CFD	$51.55 \cdot 10^{-3}$	$6.86 \cdot 10^{-3}$	1622	$1.82 \cdot 10^{9}$	$2.59 \cdot 10^{-3}$
Cantera	$51.55 \cdot 10^{-3}$	$6.86 \cdot 10^{-3}$	1631	$0.685 \cdot 10^{9}$	$2.03 \cdot 10^{-3}$

5.2.1 Fields

The distribution of H_2 is nearly identical to the distribution of NH_3 throughout the simulation. Normalized Y_{NH_3} and Y_{H_2} have practically identical values throughout all time steps, and almost

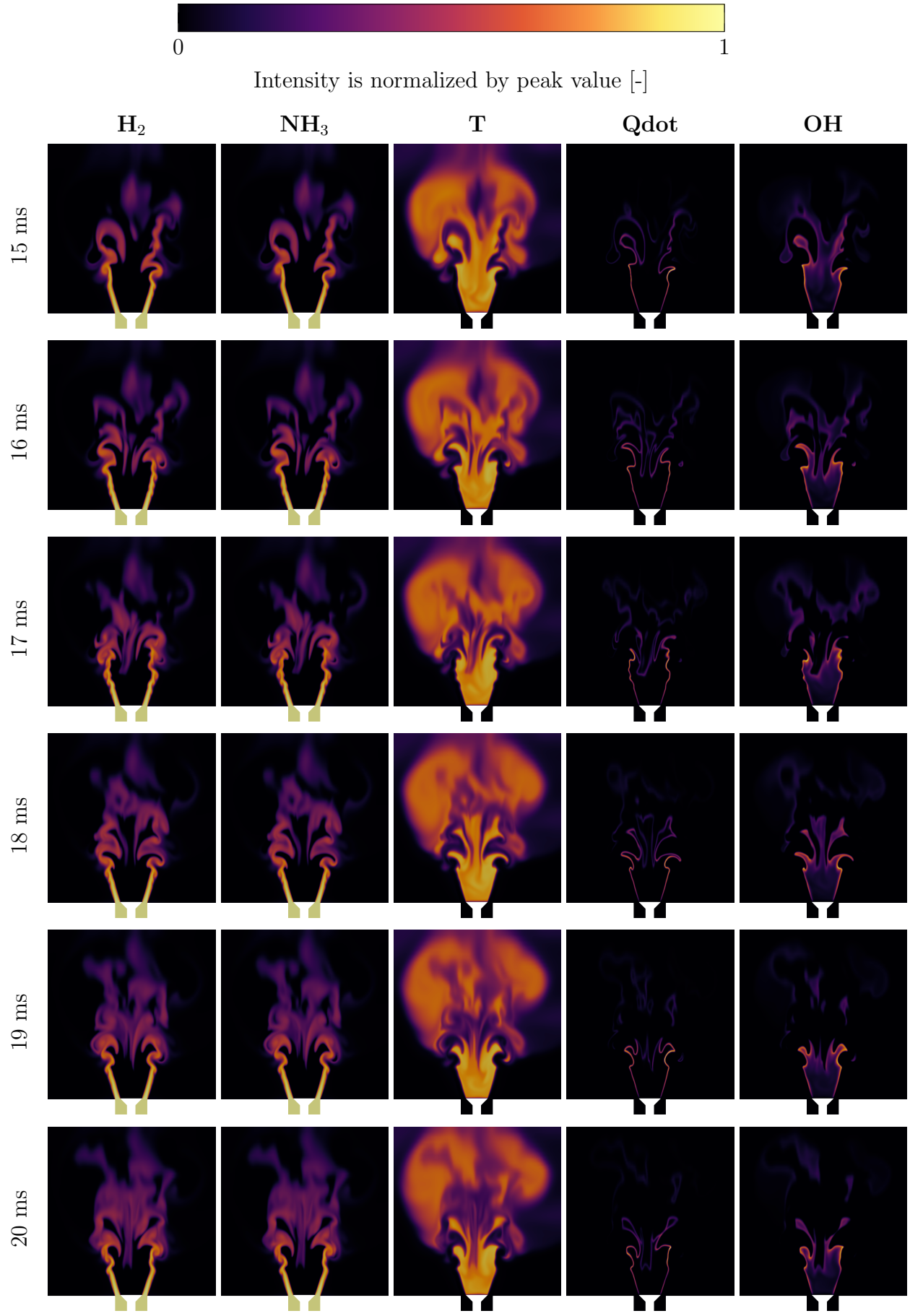

Figure 11. Time-series of instantaneous fields over different time intervals using the Vargas mechanism.

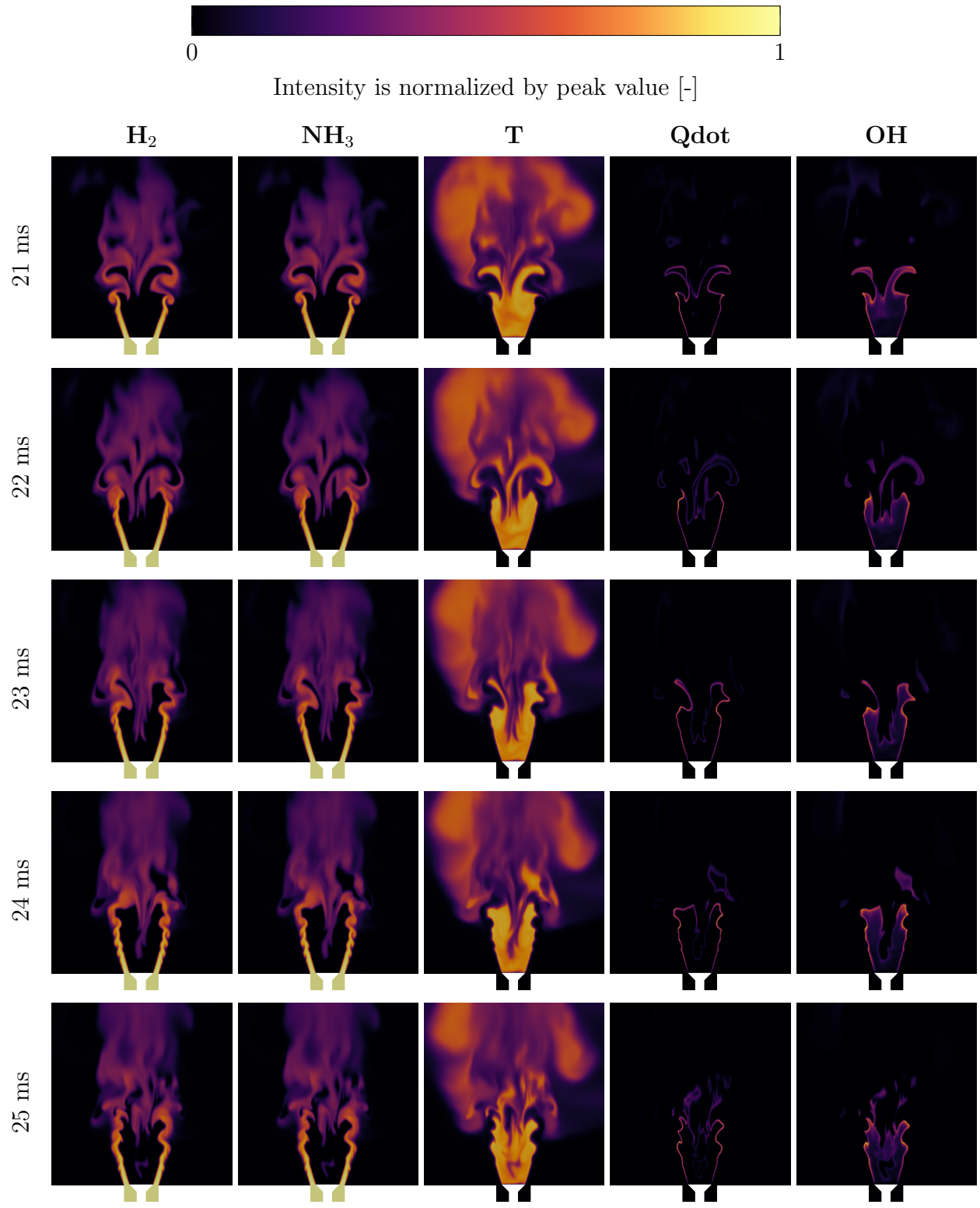

Figure 12. Time-series of instantaneous fields over different time intervals using the Vargas mechanism.

throughout the entire domain. On the product side of the flame front, Y_{NH_3} drops slightly faster than Y_{H_2} when approaching the flame front. The difference appears to reach a maximum where the intermediate species NH_2 also has a maximum concentration, right before the flame front. The distribution of reactants in the $NH_3/H_2/N_2$-air flame matches the behavior and structure of the reactants of the CH_4-air flame previously discussed. There are discrepancies. The crest of the recirculation zone is about 50 % further away from the bluff-body at blow-out than the CH_4-air flame, but the reactants of the $NH_3/H_2/N_2$-air flame appears to maintain a higher concentration of unburned reactants closer to the bluff-body for longer.

The temperature field in the recirculation zone shows spatial variance. Some cells void of unburned reactants reach temperatures as low as 1400 K, which is almost 14 % lower than the adiabatic flame temperature, as seen in table **??**. Unburned reactants caught in the cor of the recirculation zone seems to maintain a relatively low temperature of 700 K. Small spots near the surface of the bluff body also reach these cooler temperatures, though without having any unburned reactants.

Stronger HRR is found in the turbulent part of the flame front, i.e. where eddies start to form in the reactant stream. The curvature of the flame front does not appear to affect the values of HRR. Although higher HRR values are at times found where there the flame front is highly concave with respect to the product side, but similar values are also found where the flame front is slightly convex with respect to the product side of the flame front. The flame front appears to collapse inward towards the center line of the domain, as time passes. The HRR values found near the center line is significantly reduced, compared to the values found on the outside of the recirculation zone. The shortening of the flame after blow-out has started is visible through the HRR-field.

The OH distribution is found almost entirely within the volume encapsulated by the flame front. The higher values of OH is generally found where HRR is higher. The surface of the OH volume appears smooth and uncontorted until eddies form in the reactant stream. Near the crest of the recirculation zone, the Oh volume breaks up chaotically, and local Y_{OH} reduces. The M-shape in the OH field is distinct at 24 ms in figure 12.

5.3 San Diego

Finally, the numerical $NH_3/H_2/N_2$-air flame simulated with the San Diego mechanism will be presented.

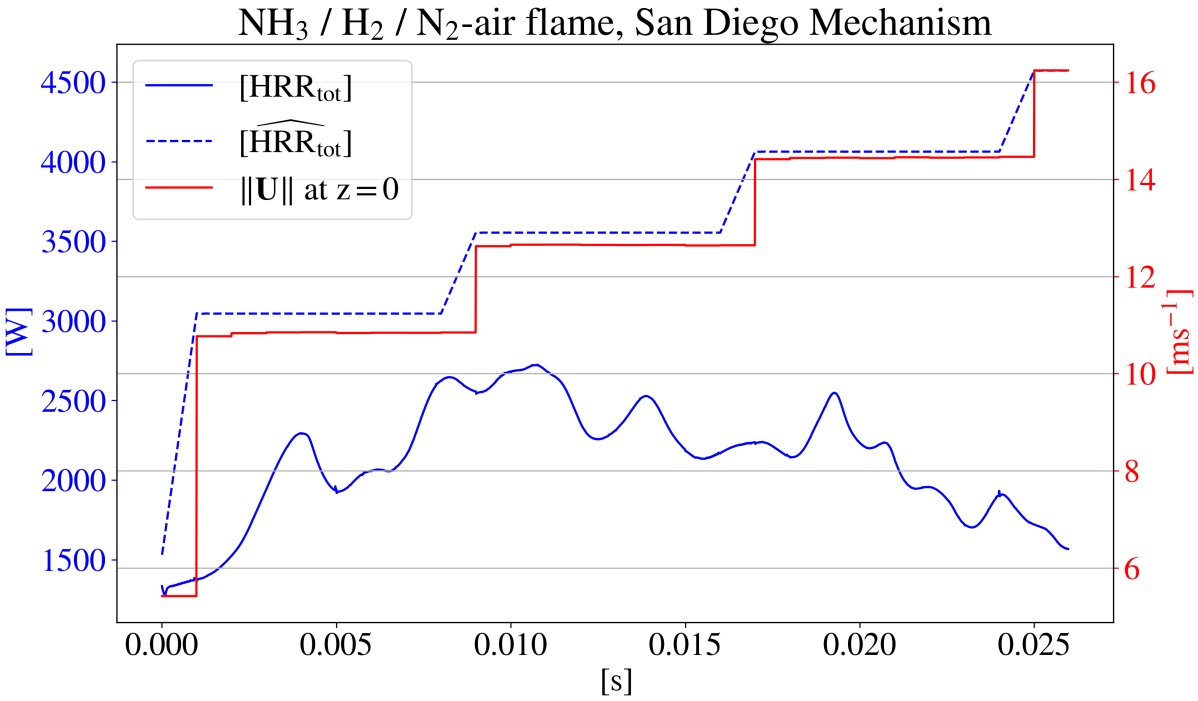

Figure 13. HRR_{tot} and $\mathbf{u}_{\text{lip}}$ over time

The peak HRR_{tot} was found just after 10 ms in Fig. 13. Before the first velocity increase, the HRR_{tot} quite differed significantly from $\widehat{HRR}_{tot}$, with 13 % relative difference. After the first increase in velocity to $||\mathbf{u}||_{lip} = 11m/s$, HRR_{tot} exhibited large oscillations in values, and came no closer than 13 % within $\widehat{HRR}_{tot}$ by the next velocity increase. After the next velocity increase to $||\mathbf{u}||_{lip} = 12.7m/s$, HRR_{tot} falls off slowly, needing almost 10 ms to reach $HRR_{tot} \leq 2000W$.

Table 10. Peak values of $NH_3/H_2/N_2$-air flame using San Diego mechanism, compared to laminar values predicted by Cantera.

	Y_{NH_3} [-]	Y_{H_2} [-]	T [K]	HRR [w/m^3]	Y_{OH} [-]
CFD	$51.56 \cdot 10^{-3}$	$6.86 \cdot 10^{-3}$	1625	$1.59 \cdot 10^{9}$	$2.53 \cdot 10^{-3}$
Cantera	$51.56 \cdot 10^{-3}$	$6.86 \cdot 10^{-3}$	1635	$0.492 \cdot 10^{9}$	$1.73 \cdot 10^{-3}$

The normalized concentration and distribution of H_2 and NH_3 appear nearly identical throughout the simulation. No qualitative differences between the two fields could be visu-

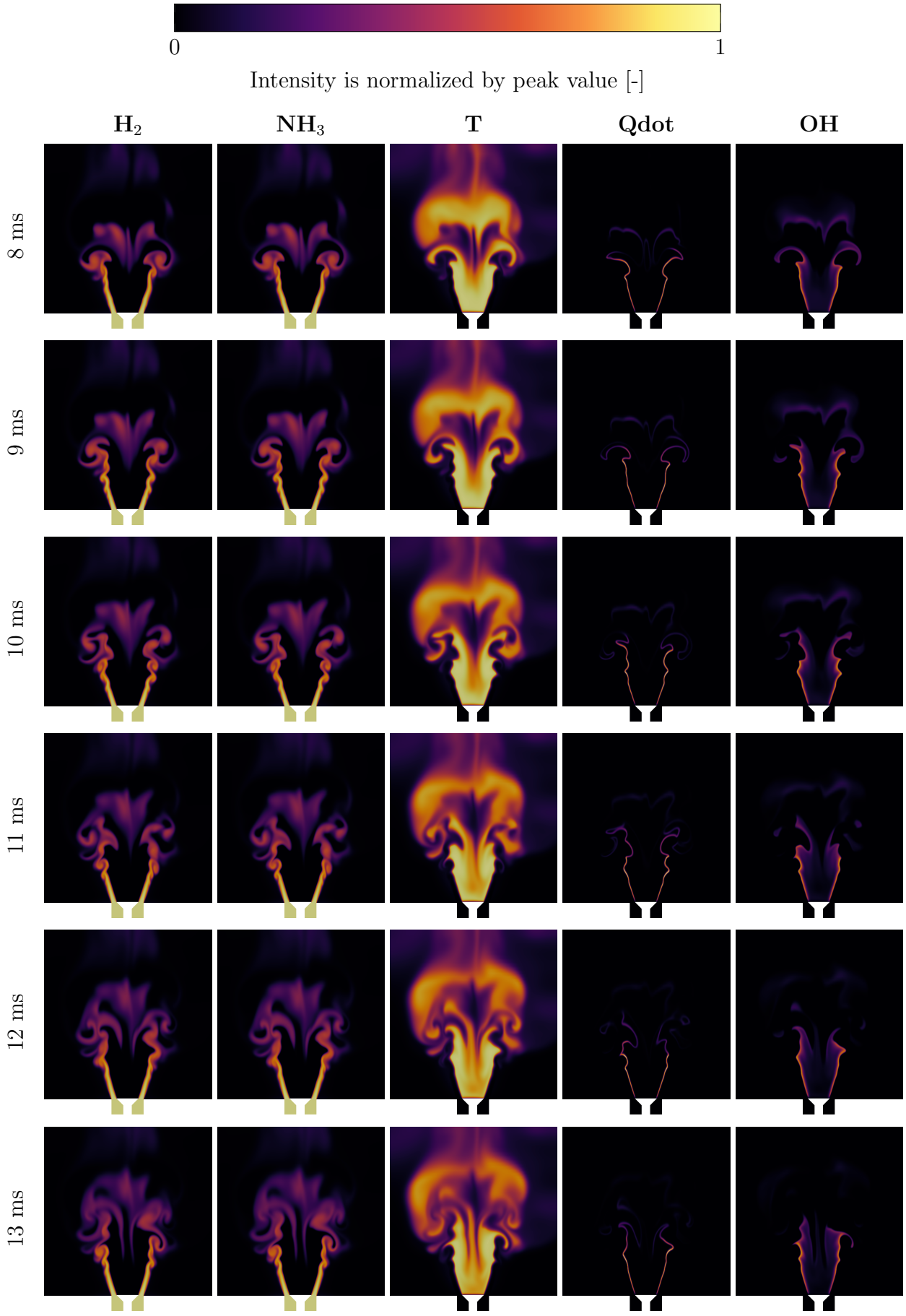

Figure 14. Time-series of instantaneous fields over different time intervals using the San Diego mechanism.

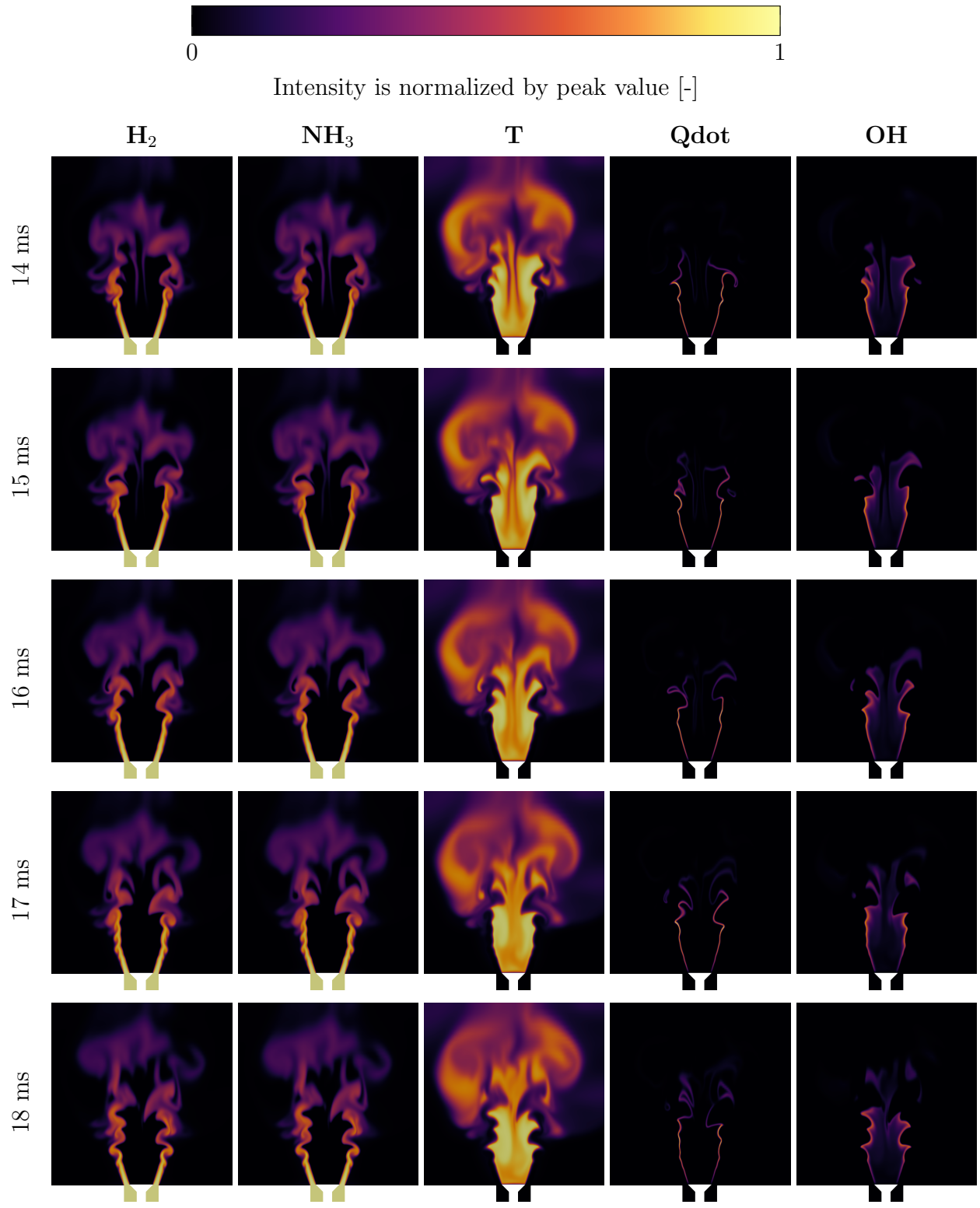

Figure 15. Time-series of instantaneous fields over different time intervals using the San Diego mechanism.

ally found. Unlike the Vargas mechanism, the reactant stream appears to appear eddy-free up to only 1 D_{BB} downstream of the bluff body. A zone with lower values Y_{NH_3} and Y_{H_2} can be found directly downstream of the recirculation zone, believed to be the result of the first increase in velocity. Columns of unburned reactants entering the core of the recirculation zone barley appears, and the columns disappear before it reaches within 1 D_{BB} of the bluff body.

After the first velocity increase, a cooler column appears to linger in the core of the recirculation zone, and gets transported down to the bluff-body. This transport of cooler gases reduces the temperature of the lower recirculation zone to about 1350 K, which is about 17 % lower than the temperature of the adiabatic flame solution.

HRR appears to be well-distributed along the flame front. No region contains any hot spots with increased HRR relative to the rest of the flame front. No correlation between local curvature in the flame front and HRR value can be observed. The flame front seems move slightly towards the center line of the domain as time passes.

OH is found mainly near the flame front and Y_{OH} appears to be more correlated with HRR than with the distance downstream. The OH front does not exhibit any wrinkling, contortion, or fragmentation beyond that of the eddies formed in the reactant stream. Due to the relatively low Y_{OH} values in the center of the recirculation zone, it is hard to make out a distinct M-shape after blowout.

6 Discussion

As mentioned in Verification and Validation, many assumptions and simplifications are made to reduce the computational cost of this investigation. Hence, discrepancies between experiments and this simulation were expected. In this section, the presented results will be discussed, and an attempt to explain why the model differs from experiments will be made. Before that, some general remarks can be made. First of all, the CH_4-air simulation came quite close to the experimental value. Hence, it can be assumed that the simulation setup and choice of models are valid for simulating a lean, premix CH_4-air flame at blow-out. To improve the accuracy of the CH_4-air flame simulation, changing smaller settings and values might be enough. Both $NH_3/H_2/N_2$-air flames underperformed poorly. This cannot be due to erronous settings. It is evident that the current simulation setup na dchoice of models is failing to capture some physics. For these flames, the current simulation setup is not valid for simulating blow-out.

6.1 Mesh

LES imposes strict mesh requirements, necessitating the resolution of at least 80 % of the turbulent kinetic energy at any point within the domain. This requirement was fulfilled in certain areas of interest where chemical activity was anticipated. However, the region surrounding the bluff body in the reactant stream did not meet this criterion, potentially resulting in the neglect of certain eddies that could impact the flame front and, consequently, the flame's behavior. However, the non-reactive simulation with finer mesh, as presented in sec. **??**, indicated that having finer cells would nelgigbly change the flow field around the bluff body. Hence, descrepancies between simulation and experiment is likely to not come from insufficient cell size around the bluff-body.

The outlet patches also failed to satisfy the 80 % turbulent kinetic energy resolution requirement. Nevertheless, given their distance from the zone of interest and their predominantly quiescent air composition, it was assumed that these areas would likely have minimal influence on the simulation results. However, it is important to note that if the simulation were to exhibit significant pressure waves that traverse between the flame and outlet patches, this would not be an acceptable compromise. Fortunately, in this case, such pressure waves were not observed, and therefore, it was deemed beneficial to reduce cell size in the vicinity of the outlet patch in order to lower computational costs.

The mesh exhibited varying cell sizes throughout the domain. Radially, this variability is a natural consequence of employing a structured mesh, as it requires the same number of

cells to cover both the outer perimeter and the smaller bluff-body lip. Vertically, a reduction in cell density was introduced intentionally to decrease the overall cell count. Although the zones of interest met the requirement of resolving at least 80 % of the turbulent kinetic energy, some chemical activity did occur within the region of lower cell density. While this region was significantly downstream of the primary chemical activity, it could still impact species distribution, eddy breakdown, and temperature gradients — important factors in predicting blowout events. As many of the simulations exhibited taller flames, compared to experiment, a finer downstream mesh might have an influence on this elongation. It is hard to say for sure without a sensitivity study on this factor.

Furthermore, extending the height of the domain to capture even more of the downstream gradient could potentially enhance the accuracy of blowout predictions. Nevertheless, it is assumed that the impact of this extension would be negligible compared to the other factors mentioned in this section.

As the experimental $NH_3/H_2/N_2$-air flame blew out at much higher velocity, Re_{exp} would also be very high. It is doubtful that the mesh would be able to resolve over 80 % of the turbulent kinetic energy at a Re of this magnitude, and so the mesh must also be reevaluated if improved diffusion and reaction models are to be tested.

6.2 Flame structure

Both the numerical CH_4-air and $NH_3/H_2/N_2$-air flames exhibited a realistic shape, consistent with theory and experiments. Immediately behind the bluff-body, a stable recirculation zone containing hot products was formed. Around the recirculation zone flowed the reactant stream, separated by a flame front that extended slightly downstream of the recirculation zone. The reactant stream became thinner with downstream distance, due to mass exchange with the recirculation zone through the flame front. The ambient air around the reactant stream had negligible mass exchange with the reactant stream. The flame front near the bluff body was smooth, uncontorted, and laminar in appearence. Further down stream, larger curves in the flame front can be found, but they were relatively stable and well-behaved. Near the top of the circulation zone, the flame front smoothly diffused, with periodic vortex formation that dispersed the hot products throughout the upper domain. The diameter of the flame front expanded slightly with downstream distance, with the shedding vortexes being significant in size relative to the diameter of the flame. At blowout, the flames appeared to be elongated compared to the flame of the experiments.

Near blow-out, all flames did exhibit a M-shape, which is in agreement with experiments [21]. This can be seen as an indication that the recirculation zone maintains moment even after peak HRR_{tot}. Near blow-out, all flames had a higher frequency of vortex shedding. This can be expected due to higher Re. The flame front also became unstable further upstream, relative to the steady-state that was used as the initial condition. At higher inlet velocities it also exhibited more asymmetric behaviour. This is consistent with experiements, and both stage one and two of the blow-out process, defined by Lieuwen [11].

The $NH_3/H_2/N_2$-air flame did not exhibit the crinkeling of the flame front, which is easily observable by Wisemans experiment. It must be remembered that the experimental flame extinguished at a much higher velocity, nearly an order of magnitude larger than the numerical one. The much higher velocity will greatly increase the presence of turbulence, but as the DNS study revealed, the crinkled flame front is a distinct feature of a low-Le premixed flame. The numerical flame was void of this.

The flame did otherwise not exhibit any features noteworthy for this study.

6.3 Velocity Increase

The magnitude and timing of the velocity increase significantly influence the contortion of the flame front. The size of the eddies that follow downstream after a velocity increase seems to scale with the velocity increase. This can be explained by the fact that as the reactant stream flow rate accelerates, the surrounding gases do not accelerate as quickly. The only reason these gases have momentum is due to momentum transfer from the reactant stream. This causes momentary shear, triggering turbulent eddies. The eddies grow in size as they travel downstream, distorting the recirculation zone as expected.

In both the CH_4-air and $NH_3/H_2/N_2$-air flames, it can be observed that eddies carrying reactants cut into the crest of the recirculation zone, introducing cold reactants into the core. This cools down the core, inhibiting reaction activity. In the CH_4-air flame, one side experiences a significant reduction in Y_{OH} after an eddy has passed over. Due to the flow direction of the core, the cold reactants will be entrained into the core. If the core does not heat up the cold reactants to reaction temperature, then the reactants will go unconsumed as they are dragged towards the bluff-body. In this case, the flame then exhibits the recognizable M-shape, as observed in simulations and reported in experiments.

Increasing the velocity to maximize shear between the reactants and products, leading to large eddies, might prematurely trigger blow-out. A more conservative approach ensuring the

momentum shear between the reactant flow and recirculation zone is smaller might provide more realistic values for blow-out velocity. The CH_4-air flame experienced the start of blow-out close to experimental values but still underpredicts the blow-out speed. A gentler velocity increase that reduces shear, might have increased the accuracy of the model.

If the flame has not experienced blow-out yet, the eddies pass by the flame, causing some unstable contortion that returns to a steady-state after an appropriate amount of time. HRR_{tot} can return to a nominal value before the flame front stabilizes itself, so the appropriate time should be based on the state of the flame front geometry, not HRR_{tot}. Increasing the inlet velocity before the flame stabilizes or the eddies from the previous velocity increase have passed causes additional eddies that further destabilize the flame and promote blow-out triggering conditions. Therefore, the time between inlet velocity increases might be too short to properly replicate the blow-out conditions of Wisemans experiment.

The combination of a large inlet velocity increase and a short stabilization time is a likely cause for why all the presented flames experienced premature blow-out compared to the experiment. It is unlikely that the premature blow-out of the $NH_3/H_2/N_2$-air flame is solely due to this, but a proper velocity increase can uncover the true influence of other simulation variables, like the lack of appropriate diffusion models.

6.4 Reactant transport

Neither of the $NH_3/H_2/N_2$-air flames showed any qualities of a low-Le premixed turbulent flame. The crinkled flame front is absent, bar large eddies further downstream above the bluff-body. It must be remembered that the visualization of the $NH_3/H_2/N_2$-air flame in Wisemans report show the flame near blow-out, which is at a much higher velocity than the simulation achieved. Therefore, some of the crinkling might simply be the result of a highly turbulent jet. The HRR plot of fig. 10 did show significant variance due to the flame front being contorted, which changed the total surface area of the flame front, which affects the total burn rate of reactants. High HRR and Y_{OH} did not track well with areas of high curvature of the flame front, which is another indication of the neglect of low-Le effects. Y_{OH} did appear stronger downstream of the bluff-body.

This is due to the oversimplified diffusion model that is the standard model in `OpenFOAM`. Fickian diffusion model, as it is implemented in `OpenFOAM`, assumes $Le \approx 1$. This disallows the natural balance between heat propagation and molecular transport, which is the fundamental mechanism that causes crinkling of the flame front, increased heat release, and hence resilience

to blow-out. The model did also not exhibit any differential diffusion between H_2 and NH_3, which occurs likely due to the mixture-averaged diffusion coefficient of the model.

6.5 Combustion model

The turbulence-chemistry interaction model used successfully produced the blow-out of the CH_4-air flame at a velocity within 10% of the experiment, which strengthens the applicability of the PaSR model for this problem. As already discussed at length, the oversimplified diffusion model used, based on Ficks law and the adhering assumptions, is seemingly the main reason for why the current setup did not manage to reproduce blowout at speeds within the same order of accuracy for the $NH_3/H_2/N_2$ air flame. While the PaSR model was sufficient for the CH_4-air flame, it must be discussed if that would also be the case for the $NH_3/H_2/N_2$-air flame given that an improved diffusion model is used; Is the diffusion model the only culprit in why the $NH_3/H_2/N_2$-air flame blew out early compared to experiment?

As explained in Chapter 2.3, the model assumes that the reaction process can be modeled as a perfectly stirred reactor, but the reaction process does not take place in the whole control volume. This is then scaled on the basis of the ratio of the chemical time scale to the turbulent time scale. This implies that the model assumes that *turbulent motion* is the dominant mode of mixing, and other modes of mixing do not affect how much of the volume experiences reactions. As previously mentioned, the diffusion of hydrogen in a mixture is significant and hence must also be considered as a mode of mixing. This is unique for hydrogen, and not as relevant for other species, such as CH_4 and NH_3. Hydrogen is also fast-reacting, implying that the turbulent time scale is not significantly bigger than the chemical time scales and hence the PaSR model will reduce the reacting cell volume fraction and hence the local burn rate in a flame.

A simplification that the PaSR model does as it is implemented in `OpenFOAM`, is to use the same reacting volume fraction κ for all species reactions, as pointed out by Arvid Åkerblom [42]. This builds on the assumption that the rate of mixing in a control volume does not differ significantly between species, as it is the turbulent interaction that is the dominant mode of mixing and transport of the whole mixture, not individual species. The differential diffusion effect is fundamentally not considered when evaluating transport mechanisms for mixing. The chemical time scale is also applied to all reactions, and taken is evaluated based on the individual reactions. The evaluation thus adapts to local variations but applies this one time scale to determine the reacting volume fraction to all reactions, despite each reaction having its own time scale.

Note that the PaSR-model does not propose any distinct standardized way to compute these time scales. The model itself only scales the reacting volume fraction based on a ration between two time scales. It is the user who must determine the relevant timescales and how to compute them themselves.

It has previously been argued by Sabelnikov & Fureby (2013) [43] that the mixing time scale τ_{mix} as follows

$$\tau_{mix} = \sqrt{\tau_k \tau_\Delta} \tag{6.1}$$

where $\tau_\Delta = \Delta/|\mathbf{u}'|$. They also suggest to define the chemical time scale τ_{chem} as follows

$$\tau_{chem} = \nu/S_{L,0}^2 \tag{6.2}$$

The reasoning is that the generally anisotropic turbulent fine structures are influenced by velocity stretch, affecting the ribbon- and tube-like structures. This assumes also uniform laminar flame speed, which would be correct to assume if the local equivalence ratio has negligible variance throughout the flame front. Differential diffusion does lead to non-uniform local equivalence ratios, and so the proposed ways of evaluating the time scales might not be applicable to lean, premixed, $NH_3/H_2/N_2$-air flames.

To address the impact of fast diffusion-induced mixing when turbulent time scale τ_{turb} exceed the diffusion time scale τ_{diff} (assuming accurate evaluation of turbulent time scale), the diffusion time scale can be used as the mixing time scale τ_{mix} in eq. (2.10. An example in how the diffusion time scale can be evaluated, is to evaluate the surface integral of diffusive fluxes of the control volume to find the mass flow due to diffusion, and divide the local mass by the diffusion mass flow, as proposed

$$\tau_{diff} = \frac{\int_{\delta V} \rho dV}{\int_{\delta A} \mathbf{n} \cdot \mathbf{J} \cdot dA} = \frac{m}{\dot{m}_{diff}} \tag{6.3}$$

where δV is the cell volume, δA is the cell surface, and $\mathbf{n}$ is the normal vector of the cell surface. It must be stated that the diffusion flux $\mathbf{J}$ is evaluated by a diffusion model, and so eq. (6.3 should be compatible with Fickian diffusion models, or more advanced diffusion models that accounts for differential fast diffusion.

The PaSR model should then use the smaller of the diffusive time scale and the turbulent time scale as the transport time scale.

$$\tau_{mix} = min\left(\tau_{turb}, \tau_{diff}\right) \tag{6.4}$$

This method does neglect any synergy between turbulent transport and diffusion transport.

As already noted, the PaSR model currently assumes that the degree of mixing is equal for all species. With preferential diffusion, this is not the case. The reacting volume fraction needs to be adapted to each reactant and reaction. This can be done by evaluating $\tau_{mix,i}$ for each specie i, and $\tau_{chem,j}$ for each reaction j, to determine a unique reacting volume fraction $\kappa_{i,j}$. This should produce a more $\overline{\dot{\omega}_i}$ of the different species, as it accounts for *differential* diffusion. This more substantial evaluation of time scales will be more costly, scaling with the number of species and reactions in the mechanism, and so will lead to increased compute time. Hence, it might simply not be worth the additional computational cost if there is no need for the substantial evaluation, like the case is for the CH_4-air flame.

It can be seen in the figure that the reacting volume fraction is around 0.95 for parts of the flame front $NH_3/H_2/N_2$-air flame. This is similar to CH_4-air flame, which, when considering the near identical laminar properties of the two reactant mixes. Neglecting the effects of differential diffusion and fast diffusion, the current simulation setup might give a lower κ, below what is representative for the $NH_3/H_2/N_2$-air flame. On the other hand, the Vargas reaction mechanism gave HRR_{tot} that is close to the theoretical heat release rate $\widehat{HRR}_{tot}$, indicating that the estimated heat release was representative. It is important to remember that the theoretical heat release is based on LHV of H_2 and NH_3 multiplied with the mass flow of each respective specie. Hence, the calculated theoretical heat release neglects any synergies that NH_3 and H_2 have when burnt together as a reactant mix. The PaSR model does HRR_{tot} of the correct order of magnitude for $NH_3/H_2/N_2$-air flame, indicating that the estimated heat release is realistic, given the correct reaction mechanism.

It must also be stated that the DNS investigation of both [2] and [8] that due to fast diffusion and preferential diffusion, the local geometry of the flame front affects the local equivalence ratio ϕ. If the curvature is at a subgrid scale, then the combustion model must also include some estimate of the local curvature and correct the output accordingly. Then again, it must be asked whether accounting for flame surface geometry is the task of the reaction model (PaSR, in this case) or a diffusion model. It can be argued that it is more appropriate to develop the diffusion model, as specie *transport* is not the task of a reaction model; The reaction model should deal only with the output of a transport model. Having the reaction model make corrections that should ahve been made in the diffusion model, might run the risk of different specie distribution depending if the reaction modeling is turned on or off for an simulation where no reaction takes place.

6.6 Reaction mechanism

The importance of the mechanism used must also be underlined once again, as the discrepancy between the Vargas and the San Diego mechanism is significant. The San Diego mechanism is developed for internal combustion engines and gas turbine burners, where the mechanism is tailored around elevated combustion pressures and reactant temperatures. Jiang et al. [35] does report with lean mixtures at atmospheric pressure and room temperature, the reaction mechanism does underpredict laminar flame speed compared to experiments. Hence, it was expected for the San Diego mechanism to underpredict the blow-out velocity. Underprediction of a whole order of magnitude cannot be caused by the reaction mechanism alone, considering that the mechanism was developed for NH_3 combustion. The Vargas mechanism is developed for a broader range of applications, and thus has a higher laminar flame velocity - believed to be closer to experimental values. Direct comparison between experimental values and numerical values for the specific mixture presented in this thesis are not availible, so further comments on if the Vargas mechanism overpredicts or underpredicts the laminar flame properties cannot be made at the time of writing. Still, the Vargas mechanism did also underpredict blowout by a whole order of magnitude. It did predict blow-out at a significantly higher velocity than the San Diego mechanism, as well as predicting a total heat release rate closer to the theoretical value. This indicates that the Vargas mechanism can be sufficient for simulation of the presented flame, given that the simulation is far from the blow-out limit. This discrepancy highlights that the mechanism is very influential in predicting blow-out. Mechanisms are also very expensive, so an evaluation of computational cost and needed accuracy should be done before starting a simulation campaign, as to not waste resources, or use an inadequate mechanism.

7 Conclusion

In this master thesis, a three-dimensional transient numerical simulation lean, premixed, bluff-body stabilized CH_4-air flame and $NH_3/H_2/N_2$-air flame under blowout conditions, using the computational fluid dynamics toolbox `OpenFOAM`. The goal of the thesis was to investigate if the model could reproduce the blowout event at the same characteristic flow velocity as reported in the experiment of Wiseman et al. (2021). The results have been quantitativly and qualitatively assessed and compared to both each other and the experiement which they numerically recreate. Large eddy simulation was used for turbulence modeling, along with Partially Stirred Reactor for turbulence-chemistry interaction. Three different chemical reaction mechanisms were used: Lu, San Diego, and Vargas.

The thermophyscial unique mehcanisms of the $NH_3/H_2/N_2$-air flame, being low-Lewis number and fast differential diffusion, was presented, along with a litterature review of blowout. Qualitative features of both were assessed. The results were also briefly compared to the adiabatic flame solution of Cantera.

The numerical blowout velocity of CH_4-air were in good agreement with the experiement, with a 10 % underprediction. The numerical blowout velocity of $NH_3/H_2/N_2$-air were severly underpredicted, by an order of magnitude. Still, blowout velocity was greatly affected by the kinetic mechanism, where Vargas mechanism outperformed the San Diego mechanism.

It is proposed that the diffusion model as it is implemented in `OpenFOAM` does not manage to capture the physics of the flame, due to assuming $Le \approx 1$. It is further hypothised that the Partially Stirred Reactor model must also be further developed to account for fast diffusion as a rate-controlling transport mechanism.

8 Future work

Future efforts should be dedicated to developing a diffusion model that can account for low Lewis number and fast differential diffusion. The model should be verified across a wider range of reactants with different Lewis-number, to assess if the model can still be applicable for mixtures with effective $Le = 1$. Lastly, the Partially Stirred Reactor should be reevaluated, and receive development efforts to account for rate-controlling diffusion.

References

[1] Agency, I. E., 2016, "World energy balances," .

[2] Wiseman, S., Rieth, M., Gruber, A., Dawson, J. R., and Chen, J. H., 2021, "A comparison of the blow-out behavior of turbulent premixed ammonia/hydrogen/nitrogen-air and methane–air flames," https://doi.org/https://doi.org/10.1016/j.proci.2020.07.011Proceedings of the Combustion Institute, **38**(2), pp. 2869–2876.

[3] Linstrom, P., 2021, "NIST Chemistry WebBook," https://doi.org/10.18434/T4D303NIST Standard Reference Database, (69).

[4] Æsøy, E., Aguilar, J. G., Wiseman, S., Bothien, M. R., Worth, N. A., and Dawson, J. R., 2020, "Scaling and prediction of transfer functions in lean premixed H2/CH4-flames," https://doi.org/https://doi.org/10.1016/j.combustflame.2020.01.045Combustion and Flame, **215**, pp. 269–282.

[5] Fritz, J., Kröner, M., and Sattelmayer, T., 2004, "Flashback in a swirl burner with cylindrical premixing zone," https://doi.org/10.1115/1.1473155Journal of Engineering for Gas Turbines and Power, **126**(2), p. 276 – 283, Cited by: 145.

[6] Lieuwen, T. C. and Yang, V., 2005, *Combustion instabilities in gas turbine engines: operational experience, fundamental mechanisms, and modeling*, American Institute of Aeronautics and Astronautics.

[7] Society, A. C., 2021, "Ammonia," `https://www.acs.org/molecule-of-the-week/archive/a/ammon` Accessed: 20th of December, 2023.

[8] Rieth, M., Gruber, A., Williams, F. A., and Chen, J. H., 2022, "Enhanced burning rates in hydrogen-enriched turbulent premixed flames by diffusion of molecular and atomic hydrogen," https://doi.org/https://doi.org/10.1016/j.combustflame.2021.111740Combustion and Flame, **239**, p. 111740, A dedication to Professor Kenneth Noel Corbett Bray.

[9] Mansour, M. S., 2003, "Stability characteristics of lifted turbulent partially premixed jet flames," https://doi.org/https://doi.org/10.1016/S0010-2180(02)00566-7Combustion and Flame, **133**(3), pp. 263–274.

[10] Shanbhogue, S. J., Husain, S., and Lieuwen, T., 2009, "Lean blowoff of bluff body stabilized flames: Scaling and dynamics," https://doi.org/https://doi.org/10.1016/j.pecs.2008.07.003Progress in Energy and Combustion Science, **35**(1), pp. 98–120.

[11] Lieuwen, T. C., 2012, *https://doi.org/10.1017/CBO9781139059961Unsteady Combustor Physics*, Cambridge University Press.

[12] Longwell, J., 1953, "Flame stabilization by bluff bodies and turbulent flames in ducts," https://doi.org/https://doi.org/10.1016/S0082-0784(53)80012-3Symposium (International) on Combustion, **4**(1), pp. 90–97, Fourth Symposium (International) on Combustion.

[13] HERBERT, M., 1960, "3 - AERODYNAMIC INFLUENCES ON FLAME STABILITY," *https://doi.org/https://doi.org/10.1016/B978-0-08-009468-7.50007-1Progress in Combustion Science and Technology*, J. DUCARME, M. GERSTEIN, and A. LEFEBVRE, eds., International Series of Monographs in Aeronautics and Astronautics, Pergamon, pp. 61–109.

[14] Plee, S. and Mellor, A., 1979, "Characteristic time correlation for lean blowoff of bluff-body-stabilized flames," https://doi.org/https://doi.org/10.1016/0010-2180(79)90007-5Combustion and Flame, **35**, pp. 61–80.

[15] Potter Jr, A. E. and Wong, E. L., 1958, "Effect of pressure and duct geometry on bluff-body flame stabilization," .

[16] Radhakrishnan, K., Heywood, J. B., and Tabaczynski, R. J., 1981, "Premixed turbulent flame blowoff velocity correlation based on coherent structures in turbulent flows," https://doi.org/https://doi.org/10.1016/0010-2180(81)90139-5Combustion and Flame, **42**, pp. 19–33.

[17] PAN, J. and BALLAL, D., *https://doi.org/https://doi.org/10.2514/6.1992-771Chemistry and turbulence effects in bluff-body stabilized flames*.

[18] Longwell, J. P., Frost, E. E., and Weiss, M. A., 1953, "Flame Stability in Bluff Body Recirculation Zones," https://doi.org/10.1021/ie50524a019Industrial & Engineering Chemistry, **45**(8), pp. 1629–1633.

[19] KUNDU, K. M., BANERJEE, D., and BHADURI, D., 1977, "Theoretical Analysis on Flame Stabilization by a Bluff-Body," https://doi.org/10.1080/00102207708946825Combustion Science and Technology, **17**(3-4), pp. 153–162.

[20] Kundu, K. M., Banerjee, D., and Bhaduri, D., 1980, "On Flame Stabilization by Bluff-Bodies," https://doi.org/10.1115/1.3230225Journal of Engineering for Power, **102**(1), pp. 209–214.

[21] Dawson, J., Gordon, R., Kariuki, J., Mastorakos, E., Masri, A., and Juddoo, M., 2011, "Visualization of blow-off events in bluff-body stabilized turbulent premixed flames," https://doi.org/https://doi.org/10.1016/j.proci.2010.05.044Proceedings of the Combustion Institute, **33**(1), pp. 1559–1566.

[22] Kariuki, J., Dawson, J. R., and Mastorakos, E., 2012, "Measurements in turbulent premixed bluff body flames close to blow-off," https://doi.org/https://doi.org/10.1016/j.combustflame.2012.01.005Combustion and Flame, **159**(8), pp. 2589–2607, Special Issue on Turbulent Combustion.

[23] Versteeg, H. K. and Malalasekera, W., 1995, *An introduction to computational fluid dynamics - the finite volume method.*, Addison-Wesley-Longman.

[24] Pope, S. B., 2000, "Turbulent flows," .

[25] Warnatz, J., Maas, U., and Dibble, R., 2006, *Combustion: Physical and Chemical Fundamentals, Modeling and Simulation, Experiments, Pollutant Formation*, Springer Berlin Heidelberg.

[26]

[27] Péquin, A., Iavarone, S., Malpica Galassi, R., and Parente, A., 2022, "The partially stirred reactor model for combustion closure in large eddy simulations: Physical principles, sub-models for the cell reacting fraction, and open challenges," https://doi.org/10.1063/5.0090970Physics of Fluids, **34**(5), p. 055122.

[28] Chomiak, J. and Karlsson, A., 1996, "Flame liftoff in diesel sprays," https://doi.org/https://doi.org/10.1016/S0082-0784(96)80088-9Symposium (International) on Combustion, **26**(2), pp. 2557–2564.

[29] Weller, H. G., Tabor, G., Jasak, H., and Fureby, C., 1998, "A tensorial approach to computational continuum mechanics using object-oriented techniques," https://doi.org/10.1063/1.168744Computer in Physics, **12**(6), pp. 620–631.

[30] Greenshields, C., 2023, *https://doc.cfd.direct/openfoam/user-guide-v11OpenFOAM v11 User Guide*, The OpenFOAM Foundation, London, UK.

[31] Kim, W.-W. and Menon, S., *https://doi.org/10.2514/6.1995-356A new dynamic one-equation subgrid-scale model for large eddy simulations.*

[32] Manion, J. A., Huie, R. E., Levin, R. D., Jr., D. R. B., Orkin, V. L., Tsang, W., McGivern, W. S., Hudgens, J. W., Knyazev, V. D., Atkinson, D. B., Chai, E., Tereza, A. M., Lin, C.-Y., Allison, T. C., Mallard, W. G., Westley, F., Herron, J. T., Hampson, R. F., and Frizzell, D. H., "NIST Chemical Kinetics Database," `https://kinetics.nist.gov/`

[33] Shy, S., Yang, S., Lin, W., and Su, R., 2005, "Turbulent burning velocities of premixed CH4/diluent/air flames in intense isotropic turbulence with consideration of radiation losses," https://doi.org/https://doi.org/10.1016/j.combustflame.2005.05.007Combustion and Flame, **143**(1), pp. 106–118.

[34] Lu, T., "Reduced mechanisms," `http://spark.engr.uconn.edu/mechs/mechs.htm`

[35] Jiang, Y., Gruber, A., Seshadri, K., and Williams, F., 2020, "An updated short chemical-kinetic nitrogen mechanism for carbon-free combustion applications," https://doi.org/https://doi.org/10.1002/er.4891International Journal of Energy Research, **44**(2), pp. 795–810.

[36] Ruiz, H. V., Laera, D., Lartigue, G., Cuif-Sjostrand, M., Valera-Medina, A., and Gicquel, L., 2024, "Extension of the dynamic Thickened Flame model for partially premixed multi-fuel multi-injection combustion - Application to an ammonia-hydrogen swirled flame," Version 2.6.0.

[37] Goodwin, D. G., Moffat, H. K., Schoegl, I., Speth, R. L., and Weber, B. W., 2022, "Cantera: An Object-oriented Software Toolkit for Chemical Kinetics, Thermodynamics, and Transport Processes," `https://www.cantera.org`, doi:10.5281/zenodo.6387882, Version 2.6.0.

[38] Lu, T. and Law, C. K., 2008, "A criterion based on computational singular perturbation for the identification of quasi steady state species:

A reduced mechanism for methane oxidation with NO chemistry," https://doi.org/https://doi.org/10.1016/j.combustflame.2008.04.025Combustion and Flame, **154**(4), pp. 761–774.

[39] Lucchese, L., 2022, "Implementation of non-reflecting boundary conditions in OpenFOAM," http://dx.doi.org/10.17196/OS$_C$FDYEAR$_2$022ProceedingsofCFDwithOpenSourceSo

[40] Iavarone, S., Péquin, A., Chen, Z. X., Doan, N. A. K., Swaminathan, N., and Parente, A., 2021, "An a priori assessment of the Partially Stirred Reactor (PaSR) model for MILD combustion," https://doi.org/https://doi.org/10.1016/j.proci.2020.06.234Proceedings of the Combustion Institute, **38**(4), pp. 5403–5414.

[41] Fureby, C., 2012, "A Comparative Study of Flamelet and Finite Rate Chemistry LES for a Swirl Stabilized Flame," https://doi.org/10.1115/1.4004718Journal of Engineering for Gas Turbines and Power, **134**(4), 041503.

[42] Akerblom, A., 2022, "Turbulence-chemistry interaction in OpenFOAM and how to implement a dynamic PaSR model for LES of turbulent combustion," http://dx.doi.org/10.17196/OS$_C$FDYEAR$_2$022ProceedingsofCFDwithOpenSourceSoftware,

[43] Sabelnikov, V. and Fureby, C., 2013, "LES combustion modeling for high Re flames using a multi-phase analogy," https://doi.org/https://doi.org/10.1016/j.combustflame.2012.09.008Combustion and Flame, **160**(1), pp. 83–96.

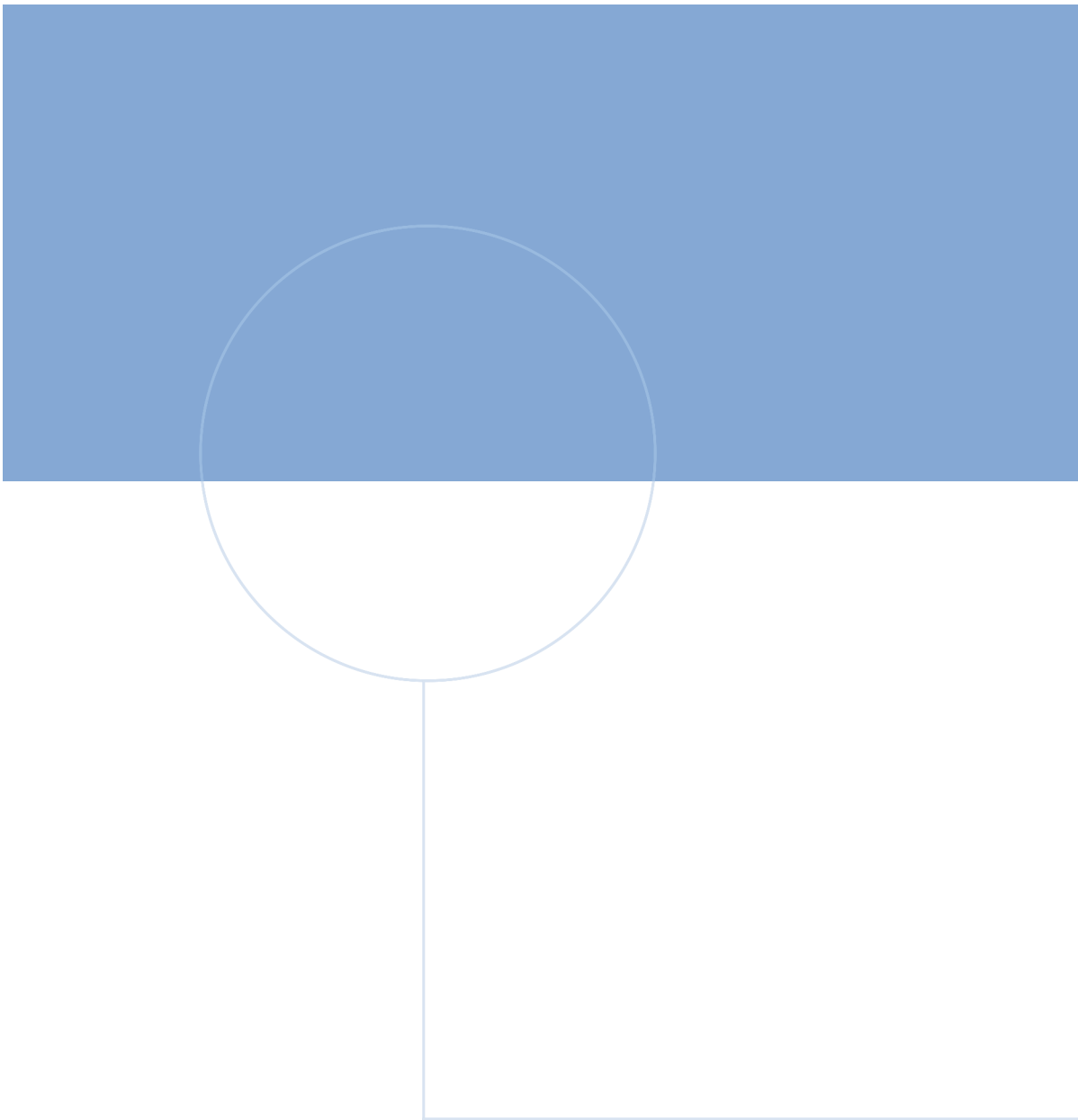

NTNU

Norwegian University of
Science and Technology